

# Chronic cAMP activation induces adipocyte browning through discordant biphasic remodeling of transcriptome and chromatin accessibility



Jisun So, Solaema Taleb, Jamie Wann, Olivia Strobel, Kyungchan Kim, Hyun Cheol Roh\*

## ABSTRACT

**Objective:** Adipose tissue thermogenesis has been suggested as a new therapeutic target to promote energy metabolism for obesity and metabolic disease. Cold-inducible thermogenic adipocytes, called beige adipocytes, have attracted significant attention for their potent anti-obesity activity in adult humans. In this study, we identified the mechanisms underlying beige adipocyte recruitment, so-called adipocyte browning, by different stimuli.

**Methods:** We generated a new adipocyte cell line with enhanced browning potentials and determined its transcriptomic and epigenomic responses following cAMP (forskolin, FSK) versus PPAR $\gamma$  activation (rosiglitazone). We performed time-course RNA-seq and compared the treatments and *in vivo* adipocyte browning. We also developed an improved protocol for Assay for Transposase Accessible Chromatin-sequencing (ATAC-seq) and defined changes in chromatin accessibility in a time course. The RNA-seq and ATAC-seq data were integrated to determine the kinetics of their coordinated regulation and to identify a transcription factor that drives these processes. We conducted functional studies using pharmacological and genetic approaches with specific inhibitors and shRNA-mediated knockdown, respectively.

**Results:** FSK, not rosiglitazone, resulted in a biphasic transcriptomic response, resembling the kinetics of *in vivo* cold-induced browning. FSK promoted tissue remodeling first and subsequently shifted energy metabolism, concluding with a transcriptomic profile similar to that induced by rosiglitazone. The thermogenic effects of FSK were abolished by PPAR $\gamma$  antagonists, indicating PPAR $\gamma$  as a converging point. ATAC-seq uncovered that FSK leads to a significant chromatin remodeling that precedes or persists beyond transcriptomic changes, whereas rosiglitazone induces minimal changes. Motif analysis identified nuclear factor, interleukin 3 regulated (NFIL3) as a transcriptional regulator connecting the biphasic response of FSK-induced browning, as indicated by disrupted thermogenesis with NFIL3 knockdown.

**Conclusions:** Our findings elucidated unique dynamics of the transcriptomic and epigenomic remodeling in adipocyte browning, providing new mechanistic insights into adipose thermogenesis and molecular targets for obesity treatment.

© 2022 The Author(s). Published by Elsevier GmbH. This is an open access article under the CC BY-NC-ND license (<http://creativecommons.org/licenses/by-nc-nd/4.0/>).

**Keywords** Beige adipocyte; Transcriptome; Epigenome; NFIL3; Cellular reprogramming; Obesity

## 1. INTRODUCTION

The global prevalence of obesity has tremendously increased over the past decades, with more than 1.9 billion people classified as overweight or obese in 2016 [1]. The obesity pandemic has been accompanied by a rise in a range of chronic metabolic disorders, including type 2 diabetes, cardiovascular and liver diseases [2]. Although major efforts have been made to mitigate obesity through lifestyle changes, such as diet control, exercise, and appetite suppression, these methods have shown limited success with high rates of the rebound, urging the development of new strategies.

Adipose tissue is a key metabolic organ controlling nutrient and energy homeostasis and is classified as having 3 distinct types. White

adipocytes store excess energy in lipids and are found throughout the body. Brown adipocytes dissipate energy as heat primarily via actions of mitochondrial uncoupling protein 1 (UCP1) and reside in the anatomically distinct interscapular region. These cells are called classical brown adipocytes. The third type of adipocytes are inducible brown adipocytes, so-called beige adipocytes, which display thermogenic capacity during cold exposure, arising within white adipose tissue (WAT), primarily in subcutaneous WAT [3]. Beige adipocyte recruitment, the process called adipocyte browning, is a transient response that can be reversed by warm conditions [4,5]. Unlike classical brown adipocytes, beige adipocytes retain a unique plasticity and are interconvertible between brown and white adipocyte states depending on the ambient temperature via epigenomic reprogramming

Department of Biochemistry and Molecular Biology, Indiana University School of Medicine, Indianapolis, IN 46202, USA

\*Corresponding author. E-mail: [hyunroh@iu.edu](mailto:hyunroh@iu.edu) (H.C. Roh).

Received August 16, 2022 • Revision received October 11, 2022 • Accepted October 18, 2022 • Available online 21 October 2022

<https://doi.org/10.1016/j.molmet.2022.101619>

## Abbreviations

$\beta$ -AR	$\beta$ -adrenergic receptor	GWAS	genome-wide association studies
ATAC-seq	assay for transposase accessible chromatin sequencing	iWAT	inguinal white adipose tissue
ATF2	activating transcription factor 2	MAP	mouse adipocyte progenitor
b-ZIP	basic leucine zipper	NFIL3	nuclear factor interleukin 3 regulated
BMI	body mass index	OCR	oxygen consumption rate
cAMP	cyclic adenosine monophosphate	PCA	principal component analysis
ChIP	chromatin immunoprecipitation	PGC-1 $\alpha$	PPAR $\gamma$ coactivator 1 $\alpha$
CREB	cAMP response element-binding protein	PKA	protein kinase A
CTCF	CCCTC-binding factor	PPAR $\gamma$	peroxisome proliferator-activated receptor $\gamma$
DEG	differentially expressed gene	Rosi	Rosiglitazone
E4BP4	E4 promoter-binding protein 4	SNS	sympathetic nervous system
FCCP	carbonylcyanide p-trifluoromethoxyphenylhydrazone	SSC	side scatter
FSC	forward scatter	SVF	stromal vascular fraction
FSK	forskolin	TF	transcription factor
		UCP1	uncoupling protein 1
		WAT	white adipose tissue

[5]. In humans, infants have classical brown adipocytes in the interscapular area [6,7] whereas adults are likely to have both classical brown and cold-inducible beige adipocytes in the supraclavicular area with the molecular features similar to those of mice [3,8–10]. The activity of these human brown adipocytes is inversely correlated with obesity and insulin resistance [11–13], suggesting their role as a new therapeutic target against obesity and metabolic diseases. However, the molecular mechanisms underlying adipocyte browning remain to be unclear.

The role of the sympathetic nervous system (SNS) and  $\beta$ -adrenergic signaling has been long appreciated in promoting adipose tissue thermogenesis in response to cold [14]. Upon exposure to cold temperature, norepinephrine is released by the SNS and works through  $\beta$ -adrenergic receptors ( $\beta$ -ARs) to activate the cyclic adenosine monophosphate (cAMP) and protein kinase A (PKA) signaling cascade [15,16]. The PKA phosphorylates p38 and cAMP response element-binding protein (CREB), all of which promote the transcription of thermogenic genes. Transcription factors and coactivators, including activating transcription factor 2 (ATF2), peroxisome proliferator-activated receptor gamma (PPAR $\gamma$ ), and PPAR $\gamma$  coactivator 1 alpha (PGC-1 $\alpha$ ), have been shown to mediate the pathways. Therefore, pharmacological activators of these pathways, including the  $\beta$ 3-AR agonist CL-316,243 [3,17], the adenylyl cyclase activator forskolin (FSK) [3,18,19], and the PPAR $\gamma$  agonist rosiglitazone (Rosi) [20], have been employed to promote adipocyte browning as an alternative to cold temperature. Despite their direct actions on the target signaling molecules, chronic administration at least for 3 days is required to induce beige adipocytes in mouse WAT [21]. This is consistent with cold-induced adipose tissue browning which requires continuous cold exposure for multiple days [22]. These findings suggest that adipose tissue browning, no matter whether cold- or chemical-induced, is a slow response which involves significant cellular differentiation and remodeling processes. It has been reported that beige adipocytes are recruited by *de novo* differentiation from adipocyte progenitor cells [21] and/or by transdifferentiation from white adipocytes during cold exposure [23]. In particular, the ability of mature white adipocytes to turn into beige adipocytes is of great interest. Activation of cAMP signaling and/or PPAR $\gamma$  induces remodeling of mature adipocytes into brown/beige adipocytes [3,20], however the molecular mechanisms underlying cellular remodeling during adipocyte browning are poorly understood. Furthermore, it is unclear how similar and distinct the adipocyte browning processes induced by different browning stimuli are.

In the current study, we generate a new immortalized mouse adipocyte progenitor cell line with enhanced browning potentials and use it to elucidate the molecular mechanisms underlying adipocyte browning in response to two different thermogenic agents, FSK and Rosi. Using time-course transcriptomic analysis, we demonstrate that chronic treatment of FSK and Rosi lead to similar thermogenic beige adipocyte states eventually after chronic treatments but via different transition processes. FSK induces a biphasic transcriptional response, contrary to a slow monophasic pattern of the Rosi response. The FSK-induced biphasic response is similar to the kinetics of *in vivo* adipose browning induced by cold temperature. We identify PPAR $\gamma$  as an essential player in the late phase of the FSK-induced browning. Also, by developing an improved protocol for assay for transposase accessible chromatin sequencing (ATAC-seq), we show the distinct impacts of FSK and Rosi treatments on the chromatin landscape during adipocyte browning. While Rosi induces minimal changes, FSK leads to significant remodeling of chromatin accessibility which precedes or persists after gene expression changes. Using motif analysis and functional assays, we identify nuclear factor, interleukin 3 regulated (NFIL3) as a new regulator of adipocyte browning.

## 2. MATERIAL AND METHODS

### 2.1. Cell culture

For the generation of immortalized mouse adipocyte progenitor (MAP) cells, inguinal WAT (iWAT) was collected from a 6-week old C57BL/6 J male mouse (Jax 000664), minced and digested in phosphate buffered saline (PBS) containing collagenase D (1.5 U/ml) and dispase II (2.4 U/ml) for 40 min at 37 °C. Digested lysate was mixed with the culture medium (Dulbecco's Modified Eagle Medium (DMEM)/F12 containing 10% FBS, 1% penicillin/streptomycin), filtered through 100  $\mu$ m cell strainers and centrifuged at 500 *g* for 5 min. The stromal vascular fraction (SVF) pellets were resuspended in the culture medium, filtered through 40  $\mu$ m cell strainers and seeded on collagen I-coated plates. Next day, the SVF cells were infected with lentivirus expressing SV40 large T antigen (GenTarget, LVP016-Neo). After 72 h of infection, the cells were sub-cultured into multiple 100 mm dishes and treated with G418 (Thermo Fisher, 10131035) at 600  $\mu$ g/ml for selection. After 10–15 days of selection, surviving individual colonies were transferred and expanded to generate monoclonal cell lines. Upon confluency, the cell lines were induced to differentiate into adipocytes with 5 mg/ml insulin, 500  $\mu$ M isobutylmethylxanthine, 1  $\mu$ M dexamethasone and 1  $\mu$ M Rosi for 2 days and then with 5 mg/ml insulin and 1  $\mu$ M

Rosi for another 2 days. One of the clones with the highest adipogenesis activity was designated as MAP cells and used for all the experiments. In subsequent culture, MAP cells were grown on standard culture dish/plates without collagen coating in the DMEM media containing 10% FBS and 1% penicillin/streptomycin. Murine 3T3L1 preadipocytes purchased from American Type Culture Collection were maintained in DMEM with 10% bovine calf serum (HyClone) and 1% penicillin/streptomycin. Two days after confluency, the cells were differentiated in the same way for MAP cells except not having Rosi in the differentiation media. To induce adipocyte browning, fully differentiated cells (at day 7–8 after differentiation) were treated with 10  $\mu$ M FSK or 1  $\mu$ M Rosi for the indicated time. For *Nfil3* knockdown experiments, lentiviral supernatants were generated by co-transfection of lentiviral *shNfil3* constructs with pM2D.G and psPAX2 plasmids in 293T cells and then collected after 48 h of transfection. Viral supernatants were incubated with differentiated MAP cells L1 adipocytes for 24 h and changed with fresh media. The infected MAP cells were used for experiments 4–5 days later. For BODIPY lipid staining, differentiated adipocytes were fixed with 10% formalin for 20 min, washed in PBS twice and stained with BODIPY (Invitrogen D3922) at 10  $\mu$ M for 30 min. After 3 washes in PBS (the first wash including Hoechst 33,342 (Invitrogen H3570) at 1  $\mu$ g/ml), the cells were imaged by a Zeiss Observer Z1 microscope and the images were processed by using ImageJ (National Institutes of Health (NIH)).

## 2.2. Cellular respiration

MAP cells were seeded (15,000–30,000 cells/well) on 24-well Seahorse microplates and differentiated as described above. On the day of experiment, the medium was replaced with XF Assay Medium (pH 7.4, Agilent) supplemented with 25 mM glucose, 1 mM pyruvate, and 4 mM L-glutamine (all from Agilent). After the plates incubated in non-CO<sub>2</sub> incubator for 1 h, the oxygen consumption rate (OCR) was measured using the XFe24 Analyzer and analyzed by the Wave 2.6 (Agilent). During assessment, test compounds were sequentially injected with following concentrations: 2  $\mu$ M oligomycin, 1  $\mu$ M carbonilcyanide p-trifluoromethoxyphenylhydrazone (FCCP), 0.5  $\mu$ M rotenone/antimycin A. OCR levels were normalized to DNA amounts per well (pmol/min/ng DNA).

## 2.3. Explant culture

iWAT were collected from 8 week-old C57BL/6 J male mice, washed in PBS, and cut into small pieces. The iWAT pieces were treated with 10  $\mu$ M FSK for the indicated time in DMEM/F-12 with 10% FBS and 1% penicillin/streptomycin.

## 2.4. Animal studies

All of the animal experiments were conducted according to procedures approved by Indiana University School of Medicine (IUSM) Institutional Animal Care and Use Committee (IACUC). Mice were housed under a 12 h light/dark cycle at 22 °C with a free access to food and water. For time-course cold exposure experiments, 6–7-week old male mice were individually housed in a rodent incubator (Powers Scientific) at 4 °C for 4 h, 24 h, or 72 h, and iWAT were dissected and used for RNA analysis.

## 2.5. Protein isolation and western blotting

Cell lysates were prepared using radioimmunoprecipitation assay (RIPA) lysis buffer (20 mM Tris pH 8, 140 mM NaCl, 1% Triton X-100, 0.1% sodium deoxycholate, 0.1% SDS, and 1 mM EDTA) supplemented with 1X EDTA-free protease inhibitor (Thermo Fisher Scientific, 78425). Protein concentrations were measured by a bicinchoninic acid (BCA) assay kit (Thermo Fisher Scientific, PI23228). Lysate samples

were separated by 4–15% gradient SDS-PAGE and transferred to polyvinylidene difluoride (PVDF) membranes (Millipore). Blots were incubated with primary and HRP-conjugated secondary antibodies and imaged using ChemiDoc (Bio-Rad). The following antibodies were used: NFIL3 (Cell Signaling Technology, 14,312), PPAR $\gamma$  (Cell Signaling Technology, 2443S), GAPDH (Cell Signaling Technology, 2118S), and UCP1 (Abcam, ab10983).

## 2.6. RNA isolation and quantitative RT-PCR

We used TRIzol (Invitrogen) for total RNA extraction from differentiated MAP cells according to the manufacturers' instructions. Extracted RNA (500 ng) was converted into cDNA using the High-Capacity cDNA Reverse Transcription Kit (Applied Biosystems). Quantitative RT-PCR (qRT-PCR) was performed using SYBR Green PCR Master Mix (Applied Biosystems) in a QuantStudio5 system. Fold change was determined using the  $\Delta\Delta$ CT method by comparing target gene expression with a reference gene 36B4 (Rplp0). The primers used for qRT-PCR are provided in [Supplementary Table S1](#).

## 2.7. RNA-seq

The extracted RNA was purified by on-column DNA digestion using a Qiagen MinElute Cleanup kit according to the manufacturer's instructions. For library construction, the purified RNA (100 ng) was processed by an NEBNext rRNA Depletion Kit (New England BioLabs, Inc.) for removing ribosomal RNA and converting to cDNA by Maxima Reverse Transcriptase (Thermo Fisher Scientific). Double-stranded cDNA was generated from the first-strand cDNA by a NEBNext mRNA Second Strand Synthesis kit following the manufacturer's instructions. After size selection using AMPure XP beads (Beckman Coulter), sequencing libraries were generated by tagmentation (Nextera XT DNA Library Preparation kit) and subsequent PCR amplification. The libraries were quantified by Qubit, analyzed by Agilent Bioanalyzer, and sequenced on an Illumina NextSeq500.

## 2.8. Nucleus isolation, sorting and ATAC-seq

Nuclear isolation and sorting were performed as previously described [5,24] with minor modifications. Differentiated MAP cells were homogenized on ice using a douncer in nucleus preparation buffer (NPB; 10 mM HEPES [pH7.5], 1.5 mM MgCl<sub>2</sub>, 10 mM KCl, 250 mM sucrose, 0.1% NP-40, and 1X Halt protease inhibitor). Homogenates were added with Hoechst 33342 for a final concentration of 1  $\mu$ g/ml and centrifuged at 200 *g* for 10 min at 4 °C. The nuclei-containing pellets were thoroughly resuspended in 500  $\mu$ l in PBS-0.1% NP-40 buffer and filtered through 40  $\mu$ m cell strainers. Resuspended nuclei were sorted using a BD FACSAria Fusion sorter, gating on FSC, SSC, and Hoechst/DAPI fluorescence. Sorted adipocyte nuclei (*n* = 10,000) were processed for ATAC-seq by using Illumina Nextera DNA Library Preparation Kit. Sorted nuclei were pelleted by centrifugation at 200 *g* for 10 min at 4 °C and tagmented using an Illumina TDE1 Tagment DNA enzyme and buffer kits in 25  $\mu$ l reaction volume (12.5  $\mu$ l 2X Tagment DNA Buffer, 1.25  $\mu$ l TDE1 enzyme, 11.25  $\mu$ l water). Tagmented chromatin was purified using a Qiagen MinElute Cleanup kit according to the manufacturer's instruction and amplified by PCR using unique barcodes and an NEBNext High-Fidelity 2X PCR Master Mix. After 12 cycles of amplification, DNA was purified using a Qiagen MinElute Cleanup kit and then processed for size selection using AMPure XP beads. The ATAC-seq libraries were quantified by Qubit and analyzed by Agilent Bioanalyzer for size distribution and sequenced on an Illumina NovaSeq. Before sequencing, we performed quantitative PCR (qPCR) with the libraries as a quality control using primers for a set of genomic regions near adipocyte-abundant genes (e.g. *Adipoq*, *Cd36*,

*Fabp4*) and negative controls targeting gene silent regions. Chromatin accessibility was determined by fold changes using the  $\Delta\Delta\text{CT}$  method by comparing the enrichment of target loci in comparison with the negative control primers. The primers used for ATAC-seq qPCR are provided in [Supplementary Table S1](#).

### 2.9. Bioinformatics analysis

For RNA-seq data analysis, sequencing reads were pre-processed by fastp [25] for quality control, adaptor trimming, and filtering and then aligned to the mm10 mouse genome using STAR [26]. Subsequently, the filtered reads were assigned to transcriptome and quantified by featureCounts [27]. Differential gene expression analysis was conducted by edgeR [28] after the removal of lowly expressed genes (average CPM < 1). We used a fold change (FC) cutoff of  $\log_2\text{FC} > 1$  and a false discovery rate (FDR) cutoff of  $\text{FDR} < 0.05$ . Pathway analysis was conducted using Metascape [29]. Morpheus (<https://software.broadinstitute.org/morpheus/>) was used to visualize heatmaps and the Pearson correlation matrix and to perform K-means clustering. Volcano plots were drawn by a Bioconductor package EnhancedVolcano [30] in R. Correlations between the fold changes in two different conditions were calculated by the Pearson's correlation coefficient.

For ATAC-seq analysis, raw sequencing reads were processed by fastp [31] for quality control, adapter trimming, and filtering, and then aligned to the mm10 mouse genome using Bowtie2 [32]. After PCR duplicates and low-quality reads were removed by Picard (<http://broadinstitute.github.io/picard/>), reads were processed by SAMtools [33] and subject to peak-calling by MACS2 [34]. The reads assigned to peaks were quantified using featureCounts [27], and further differential analysis was conducted by edgeR only using the peaks with  $\log\text{CPM} > 1$  across all samples [28]. The same criteria as in RNA-seq analysis were used to identify differentially expressed peaks:  $\log_2\text{FC} > 1$  and  $\text{FDR} < 0.05$ . Heatmaps and the Pearson correlation matrix of ATAC-seq peaks were made using Morpheus. The ATAC-seq signal tracks were visualized by the WashU Epigenome Browser [35] using BigWig files generated by BEDTools [36] and bedGraphToBigWig [37]. The BigWig files were normalized based on the library size. Peak-to-gene annotation and *de novo* motif discovery were conducted by HOMER v4.11 [38].

### 2.10. Statistical analysis

We used two-sided Student's *t*-test, two-way ANOVA with Tukey's post-hoc test, and one-way ANOVA with Dunnett's post-hoc test, and  $P < 0.05$  was considered statistically significant.

### 2.11. Data availability

The raw and processed data of the RNA-seq (GSE214596) and ATAC-seq (GSE214597) in this paper are available in the Gene Expression Omnibus (GEO) repository (GSE214598).

## 3. RESULTS

### 3.1. Immortalized mouse adipocyte progenitor cells have improved browning capability

To develop an *in vitro* cell culture system for adipocyte browning, we isolated SVF from iWAT of C57BL/6 J mouse and immortalized it using SV40 large T antigen. After continuous passaging and single colony selection, we isolated multiple clonal immortalized cell lines, which were subsequently screened for their adipogenic potentials. One of the cell lines, we call mouse adipocyte progenitor (MAP) cells, showed high adipogenesis efficiency after differentiation induced, displaying

multilocular lipid droplets larger than the ones of 3T3L1 cells (Figure 1A). Gene expression analysis found that differentiated MAP cells, compared to 3T3L1 cells, express substantially higher levels of thermogenic and mitochondrial genes, including *Ucp1*, *Pgc1a*, *Elovl3*, *Cox7a1*, *Cox8b*, *Cidea* and *Prdm16* (Figure 1B), while expressing comparable or slightly lower levels of general adipocyte marker genes, such as *Adipoq*, *Fabp4* and *Plin1* (Figure 1C). We noted that MAP cells express significantly higher levels of *Lep*, which encodes the hormone Leptin, (Figure 1C), a marker abundant *in vivo* WAT but barely expressed in cultured adipocyte cell lines [24]. MAP cells also expressed marker genes specific for iWAT, including *Shox2*, *Tbx1*, and *Hoxc9* [5], which were absent in 3T3L1 cells (Figure 1D). These results suggest that MAP cells, retaining thermogenic potentials of iWAT, are closer to *in vivo* beige adipocytes compared to 3T3L1 cells.

To determine how differentiated MAP cells respond to environmental cues known to induce adipocyte browning, we assessed the induction of thermogenic gene expression in MAP versus 3T3L1 cells after treatment with Rosi or FSK. A 24 h Rosi treatment resulted in a significant induction of all the thermogenic and mitochondrial genes in MAP cells, but minimal changes were found in 3T3L1 cells (Figure 1E). Both types of cells exhibited a comparably mild induction of general adipocyte marker genes, except that *Fabp4* was highly induced in MAP cells only (Figure 1F). UCP1 protein was more abundant in MAP cells at the basal state and significantly upregulated by the Rosi treatment in MAP but not in 3T3L1 cells (Figure 1G). On the other hand, PPAR $\gamma$  protein levels were reduced both in MAP and 3T3L1 cells presumably by a feedback mechanism of Rosi-driven PPAR $\gamma$  activation [39] (Figure 1G), indicating that the cell line-dependent differences reside specifically in thermogenic gene expression profile, not the global cellular responsiveness. Also, in response to a treatment with FSK for 4 h, MAPs displayed a strong induction of a set of thermogenic genes, such as *Ucp1*, *Pgc1a*, *Dio2*, and *Elovl3*, whereas 3T3L1 did not robustly respond, as only *Pgc1a* and *Dio2* were moderately induced (Figure 1H). Taken together, these results indicate that differentiated MAP cells are better for activating thermogenic cellular programs upon pro-browning stimuli than 3T3L1. However, an unexpected finding was that some thermogenic genes, which especially encode structural proteins essential for thermogenesis, such as mitochondrial respiration complex proteins (*Cox7a1* and *Cox8b*) and lipid droplet proteins (*Cidea*), were not induced and rather downregulated within 4 h of FSK treatment in both MAP and 3T3L1 cells (Figure S1A). The expression of general adipocyte marker genes also decreased in a similar manner (Figure S1B). These results suggest that acute cAMP activation induces a distinct gene expression profile compared to the browning state induced by PPAR $\gamma$  activation.

### 3.2. Chronic cAMP activation induces functional adipocyte browning via biphasic response

To characterize the kinetics of the adipocyte browning process induced by FSK and Rosi, we conducted a time-course assessment of gene expression following either treatment for 5 days in differentiated MAP cells. Intriguingly, chronic FSK treatment, unlike Rosi, triggered a biphasic response in MAP cells. During the 1st phase (0–24 h after stimulation), a set of thermogenic genes (e.g. *Ucp1*, *Pgc1a*, *Dio2*) were acutely induced within 2–4 h but shortly came back down comparable to the baseline levels toward 24 h, while the other set of thermogenic genes (e.g. *Cox7a1*, *Cox8b*, *Cidea*) and general adipocyte markers (e.g. *Adipoq*, *Plin1*, *Fabp4*) were barely affected or rather decreased (Figure 2A). After 24 h of stimulation, during the 2nd phase, the expression of both thermogenic and general adipocyte marker genes started to rebound and/or increase continuously until 120 h

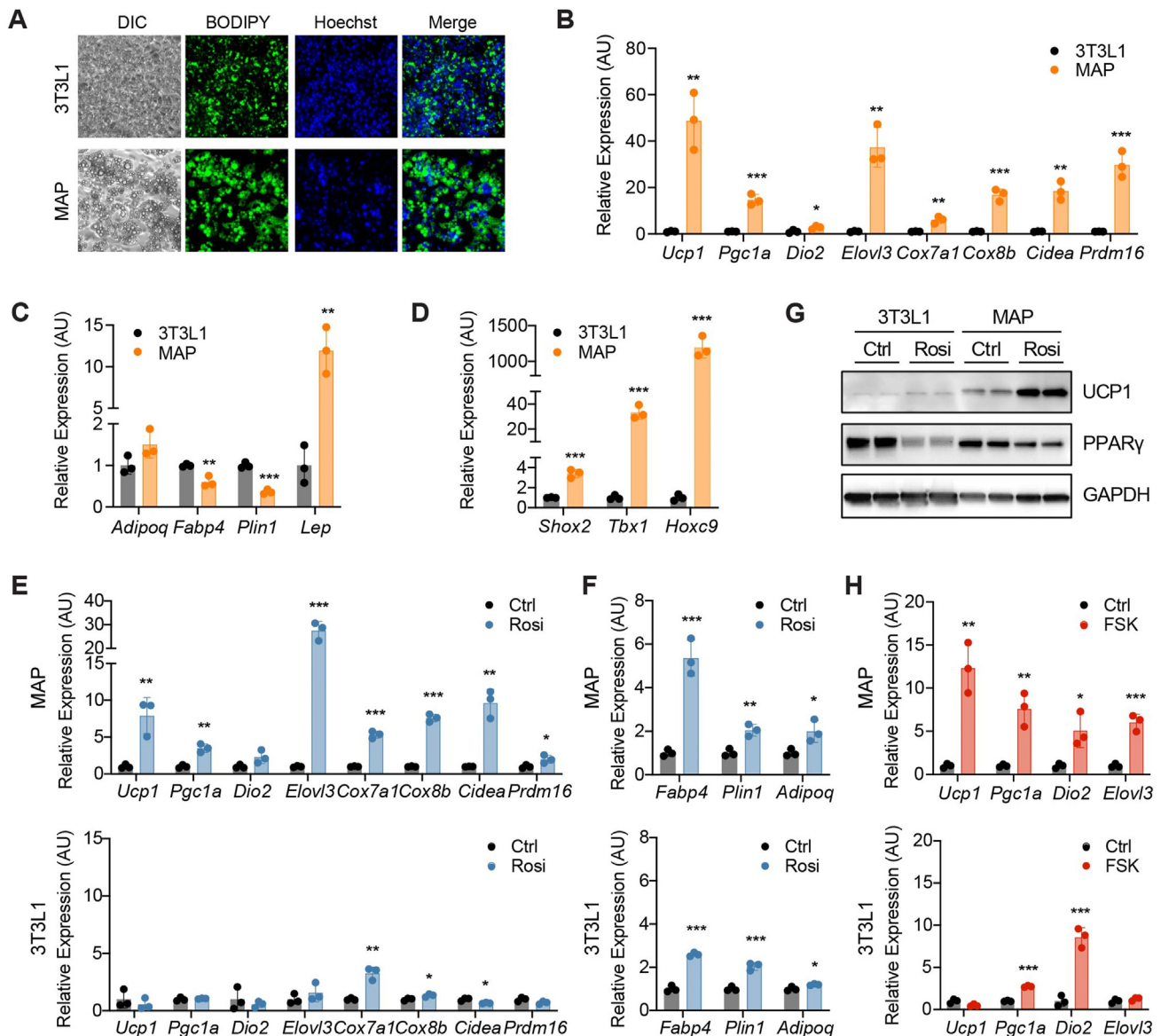


**Figure 1: Characterization of browning potentials of differentiated 3T3L1 vs. MAP adipocytes.** (A) Differential interference contrast (DIC) and fluorescence images of differentiated 3T3L1 and MAP cells. Cellular lipids visualized by BODIPY staining (green) and nuclei visualized by Hoechst staining (blue). (B–D) Gene expression analysis by qRT-PCR of thermogenic markers ( $n = 3$ ) (B), general adipocyte markers ( $n = 3$ ) (C), and subcutaneous fat-specific markers ( $n = 3$ ) (D) in differentiated 3T3L1 and MAP cells. (E–F) Effects of Rosi on the expression of thermogenic marker genes (E) and general adipocyte markers (F) genes in differentiated MAP (top,  $n = 3$ ) and 3T3L1 (bottom,  $n = 3$ ) cells. Differentiated MAP or 3T3L1 cells were treated with Rosi (1  $\mu$ M) for 24 h. (G) Protein levels of UCP1 and PPAR $\gamma$  in differentiated 3T3L1 and MAP cells with and without Rosi (1  $\mu$ M) treatment for 24 h. GAPDH was used as a loading control ( $n = 2$ ). Note the faint non-specific band below the UCP1 band. (H) Effects of short-term 4 h FSK treatment (10  $\mu$ M) on the expression of thermogenic marker genes in differentiated MAP (top,  $n = 3$ ) and 3T3L1 (bottom,  $n = 3$ ) cells. Data are presented as mean  $\pm$  standard error of the mean (SEM). Statistical analysis was performed by two-sided Student's  $t$ -test (\* $P < 0.05$ ; \*\* $P < 0.01$ ; \*\*\* $P < 0.001$ ).

(Figure 2A). However, Rosi treatment showed a distinctly slow monophasic response. Most of the thermogenic and adipocyte maker genes were gradually induced, starting from 24 h until 120 h (Figure 2B). The similar biphasic response was also observed in iWAT upon *ex vivo* FSK stimulation (Figure S2A). To determine the type of kinetics which better resembles the *in vivo* cold-induced adipocyte browning process, we exposed mice to cold temperatures (4  $^{\circ}$ C) for 72 h and analyzed iWAT gene expression at multiple time points. Akin to the FSK response, two distinct groups of thermogenic genes were induced at different times. *Ucp1*, *Pgc1a*, and *Dio2* were rapidly induced at 4 h, whereas *Cox7a1*, *Cox8b*, and *Cidea* were elevated slowly after

at least 24 h of cold exposure (Figure S2B). The adipocyte marker gene *Fabp4* also tended to be slightly induced during the 2nd phase after 24 h of exposure (Figure S2B). These results suggest that chronic cAMP activation, rather than PPAR $\gamma$ -activating Rosi, may better mimic the cold-induced browning process *in vivo*.

To determine functional thermogenesis in the course of FSK-induced response in differentiated MAP cells, we first measured UCP1 protein levels at different time points throughout the 5 d treatment. The UCP1 protein became highly abundant after longer treatments, particularly at 120 h (Figure 2C). Notably, the UCP1 protein was not detected at 4 h, the early time point where *Ucp1* mRNA was robustly

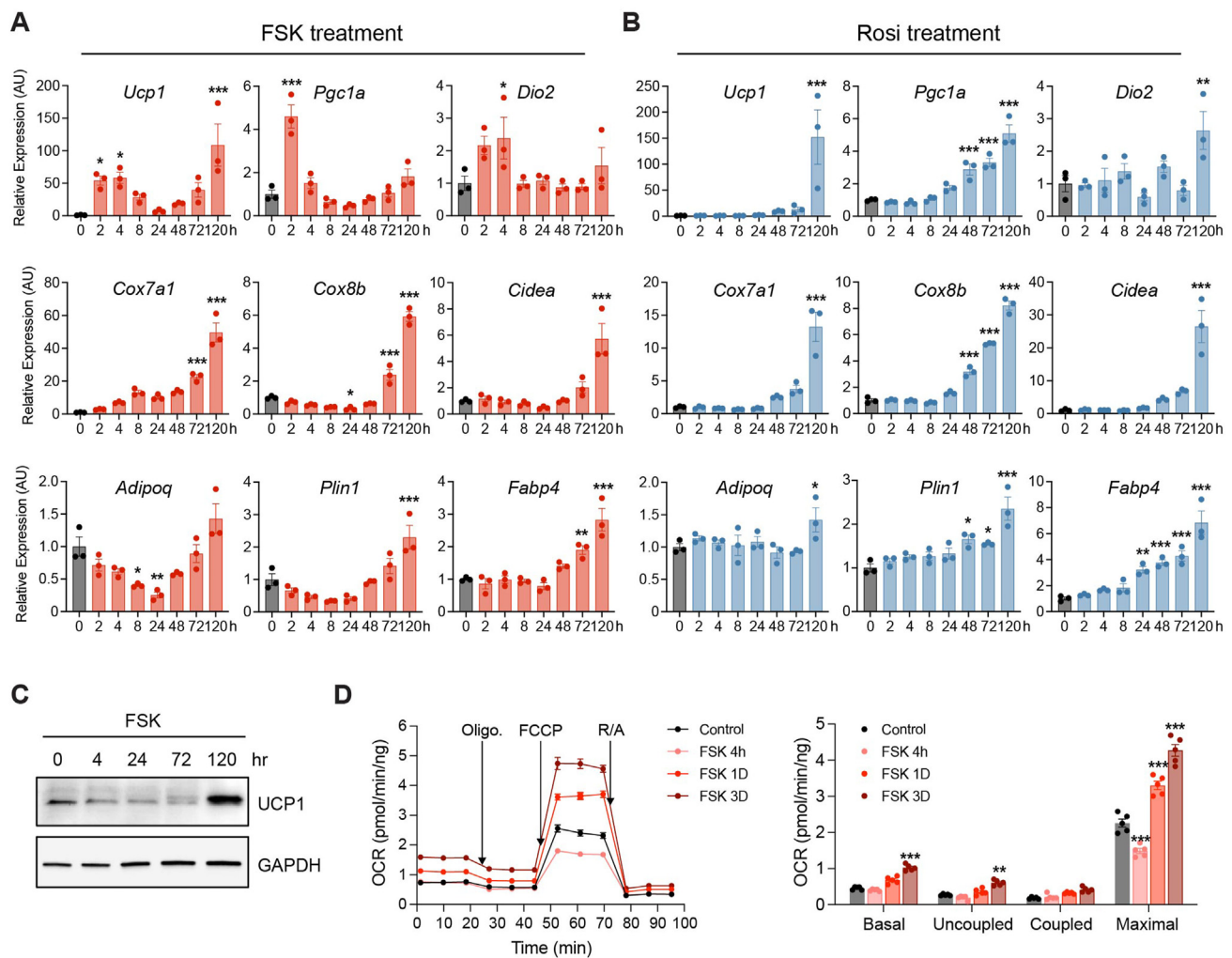


**Figure 2: Biphasic response specific to FSK stimulation in differentiated MAP adipocytes.** (A–B) Time-course response of differentiated MAP cells to FSK and Rosi treatment ( $n = 3$ ). Expression of a set of thermogenic genes (top), structure-associated thermogenic genes (middle), general adipocyte marker genes (bottom) at baseline and at the indicated time points after treatment with FSK (A) and Rosi (B). (C) Protein levels of UCP1 in response to FSK treatment at baseline and at the indicated time points. GAPDH was used as a loading control. Note the faint non-specific band below the UCP1 band. (D) Oxygen consumption rate (OCR) in differentiated MAP adipocytes treated with FSK for 0 h, 4 h, 1D, and 3D measured by a Seahorse XFe24 Analyzer ( $n = 5$ ). Bar graphs indicate quantification of basal, uncoupled, and maximal mitochondrial respiration. Data are presented as mean  $\pm$  SEM. Statistical analysis was performed by one-way ANOVA with Dunnett's post-hoc test (A–B) and two-way ANOVA with Tukey's post-hoc test (D) (\* $P < 0.05$ , \*\* $P < 0.01$ , \*\*\* $P < 0.001$  relative to control).

induced. In addition, only the FSK treatments longer than 24 h (i.e. for 1 d or 3 d) resulted in a significant increase in basal, uncoupled, and maximal mitochondrial respiration, measured by Seahorse assays (Figure 2D). The short-term 4 h treatment rather inhibited the respiration. Altogether, these data indicate that a functional induction of browning by FSK in differentiated MAP cells is not achieved by acute responses and requires a longer time enough for thermogenic genes to be fully augmented.

### 3.3. Dissection of the biphasic transcriptomic response during FSK-induced adipocyte browning

We next sought to comprehensively characterize the biphasic adipocyte browning induced by chronic FSK treatment and compare this process to Rosi-induced browning. To this end, we performed RNA-seq on differentiated MAP cells treated with FSK for multiple different durations or with Rosi for 3 days. We identified a total of 2,941 differentially expressed genes (DEGs) upon FSK or Rosi treatment and

biological pathways enriched in those gene sets (Figure S3A). The 4 h FSK treatment upregulated genes involved in vascularization, cell proliferation/differentiation and inflammation, and downregulated genes involved in cytoskeletal organization. Similar sets of pathways were enriched in the genes altered by 1 d FSK treatment (Figure S3A). These changes may represent tissue remodeling, which occurs during the early phase of *in vivo* cold-induced adipose browning [40,41]. It was not until 3 days after FSK treatment that the genes related to pathways of lipid and carbohydrate metabolism were upregulated along with a marked increase of thermogenic marker gene expression (e.g. *Ucp1*, *Cox7a1*, and *Elovl3*). These pathways activated at the earlier phase were rather repressed during chronic FSK treatment. In a similar manner, 3 d Rosi treatment activated cellular metabolism pathways and inhibited cell mitosis and vascularization (Figure S3A). The unique dynamics of FSK-induced adipocyte response is well plotted in the principal component analysis (PCA) of transcriptomic profiles (Figure 3A). Chronic treatment with FSK altered the profile in

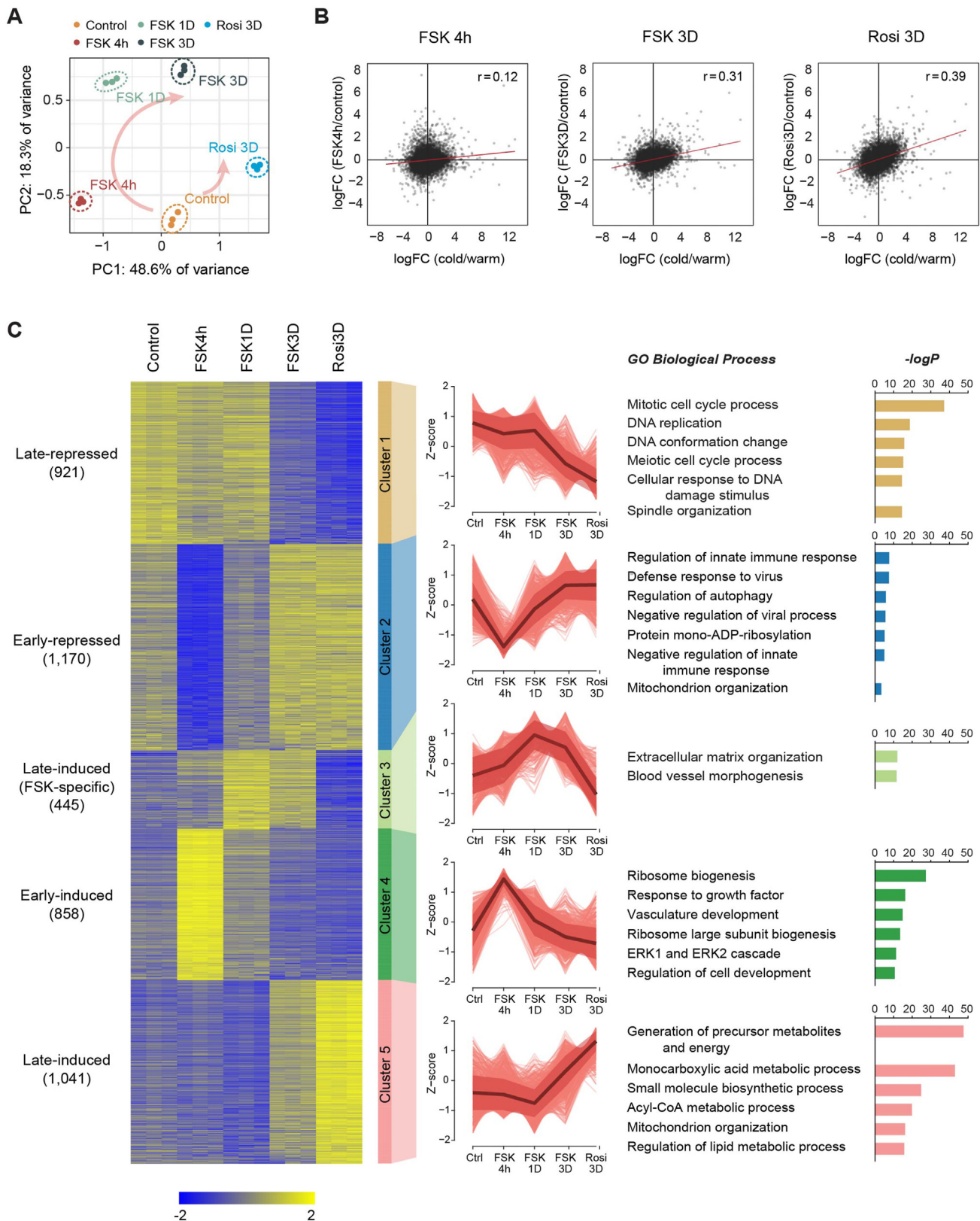


**Figure 3: Biphasic transcriptomic changes during FSK-induced adipocyte browning.** (A) PCA of transcriptome of adipocytes treated with FSK or Rosi. Each dot indicates an individual biological replicate ( $n = 3$ ). (B) Scatterplot showing correlation of fold changes of the differentially expressed genes (DEGs) upon FSK or Rosi treatment in differentiated MAP cells versus those upon cold exposure ( $4\text{ }^{\circ}\text{C}$  for 7 d) in beige adipocytes *in vivo* by TRAP RNA-seq. The red lines represent the trends. (C) Heatmap of relative expression (Z-score) of DEGs (rows) across samples (columns). Genes are classified into 5 clusters by K-means clustering based on their patterns as labeled. Parallel coordinate plot on the right shows the Z-score trends of individual gene expression across conditions per cluster. The black solid line and the ribbon indicate mean and standard deviation (SD), respectively. Pathways (Gene Ontology (GO) biological process) enriched in each cluster and their corresponding  $-\log_{10}P$  values are shown in the table on the far right.

the same direction as Rosi, compared to the basal state, but going through distinct transition states located in the opposite side during the early phase (i.e., 4 h and 1 d). These results could imply dynamic cellular remodeling processes occurring in the course of persistent cAMP stimulation as in cold-induced adipose browning *in vivo*.

Based on the findings above, we next compared transcriptomic changes made during adipocyte browning *in vitro* induced by FSK or Rosi versus *in vivo*. We previously generated beige adipocyte-specific *in vivo* RNA-seq data in response to cold or warm temperature without confounding effects from other cell types by using ribosome pulldown [5]. We used *Ucp1-Cre: NuTRAP* (NUclear tagging and Translating Ribosome Affinity Purification) mice, where the ribosomes only in *Ucp1*-expressing adipocytes were labeled with green fluorescent protein (GFP), allowing beige adipocyte-specific ribosome isolation and gene expression profiling [5]. Using these data, we determined the correlations between the fold changes of gene expression in MAP cells during FSK treatment and those in beige adipocytes during 7 d cold challenge. Started from a very weak correlation at 4 h, FSK treatment came to resemble *in vivo* response further with a longer period (i.e., 3 d) (Figure 3B). This explains that a longer treatment, at least for 3 days, is required to mimic *in vivo* adipocyte browning processes through cAMP activation. The slightly higher correlation observed between Rosi-induced and the *in vivo* response indicates that Rosi can attain, at a moderate level, the final thermogenic state achieved by cold exposure but not mimicking its biphasic response (Figure 3B). To further characterize similarities and differences between *in vitro* and *in vivo* adipocyte browning processes, we first identified a list of genes differentially expressed during either 3 d FSK treatment or 7 d cold challenge and then determined the concordance of their fold changes made in the two systems. The gene set upregulated both *in vitro* and *in vivo* was enriched with carbohydrate and lipid metabolism, while pathways of amino sugar metabolism, blood vessel organization, response to wounding (related to cell adhesion) were downregulated in both (Figure S3B). The way adipocytes metabolize fuels and interact with the surrounding environments was altered commonly during *in vivo* and *in vitro* browning processes, suggesting it as a core part of adipocyte browning. On the other hand, the genes up- and down-regulated specifically *in vivo* were related to mitochondrial organization and cell cycle process, respectively (Figure S3B), indicating a higher mitochondrial capacity and a tighter control of cell proliferation of *in vivo* beige adipocytes compared to immortalized cell lines. Conversely, some lipid handling and cellular morphology regulatory pathways were enriched only *in vitro*. Also, other pathways involved in angiogenesis, cell secretion and signaling responded in the opposite manner between *in vitro* and *in vivo* (Figure S3B). Overall, chronic FSK treatment can promote adipocyte browning as an alternative to cold temperature by mainly altering energy metabolism but producing distinct cellular responses as shown in the disagreeing transcriptomic changes.

To elucidate the biological pathways mediating the biphasic remodeling process during FSK-induced adipocyte browning, we performed K-means clustering analysis with 2,941 DEGs identified from the time-course RNA-seq data. Five major gene clusters were characterized based on their expression patterns across the conditions (Figure 3C). Gene Clusters 2 and 4 responded at the early (1st) phase of FSK treatment, being repressed and induced relative to control, respectively. On the other hand, Gene Clusters 1 and 3/5 were suppressed and increased, respectively, at the later (2nd) phase. Of note, all gene clusters displayed a common responsiveness to the chronic treatments with FSK and Rosi except Cluster 3, which was only induced by FSK, not Rosi (Figure 3C). Pathway analysis demonstrated that the early

response gene clusters (Clusters 2 and 4) were enriched with biological processes involved in immune signaling, autophagy, ribosome biogenesis, growth factor response, and vascularization (Figure 3C). The late responses included induction of genes related to energy metabolic processes and mitochondrial organization (Cluster 5) and inhibition of genes mostly involved in cell cycle and DNA regulation (Cluster 1) (Figure 3C). Taken together, cAMP-driven adipocyte browning is accomplished through tissue remodeling processes at early stages and subsequently through activation of cellular metabolism and cell cycle inhibition.

#### 3.4. Chronic FSK treatment induces gene expression changes similar to, but distinct from, rosi treatment

The resemblance between the responses following chronic FSK and Rosi treatments is indicated from their comparable correlations with *in vivo* cold response (Figure 3B) and similar gene expression profiles (Figure 3C). This suggests that FSK- and Rosi-induced browning share common molecular mechanisms during long term treatments. Consistently, a global pairwise correlation analysis of the RNA-seq data showed that 3 d FSK treatment results in the most similar transcriptomic profile to that of 3 d Rosi treatment (Figure 4A). A direct comparison between 3 d FSK- and Rosi-treated adipocytes exhibited a strong correlation ( $r = 0.66$ ), with the concordant upregulation of genes involved in monocarboxylic acid metabolism, adaptive thermogenesis and fat cell differentiation and the repression of genes related to the development of vasculature and connective tissues (Figure 4B). These results demonstrate that the core mechanisms shared during adipocyte browning driven by cAMP and PPAR $\gamma$  activation are stimulation of cellular metabolism and tissue reorganization. Rosi is a PPAR $\gamma$  agonist working in a specific mechanism by which it directly binds to PPAR $\gamma$  and activates its activity, unlike FSK exerting broader and more dynamic effects. This led us to the hypothesis that the later part of the biphasic response induced by chronic FSK treatment eventually converges to PPAR $\gamma$  activation to propel energy metabolism toward thermogenesis. To test this hypothesis, we treated differentiated MAP cells with PPAR $\gamma$ -specific antagonists, GW9662 or T0070907, during FSK-induced browning. The PPAR $\gamma$  antagonists significantly abolished the induction of all thermogenic gene expression (Figure 4C,D), manifesting that PPAR $\gamma$  activation is an important process essential for FSK-induced adipocyte browning.

Despite the similarity between FSK- and Rosi-treated adipocytes, they still displayed distinct gene expression profiles as identified in DEGs from the direct pairwise comparison: 489 and 290 genes were more expressed in FSK- and Rosi-treated cells, respectively (Figure 4E). Compared to Rosi, FSK elicited cell migration/adhesion and inflammatory response (Figure 4E), suggesting that inflammation-related signaling is a unique mechanism of cAMP-induced adipose tissue browning. Conversely, Rosi induced pathways involved in metabolism of nutrients, including lipids, to a greater extent than the long-term FSK treatment (Figure 4E; Figure S3A). This indicates that these lipid metabolism-related gene sets are the direct targets of Rosi, which FSK can activate in the long term. The addition of minimal doses of Rosi at 10 nM or 100 nM to FSK treatment further enhanced thermogenic gene expression substantially (Figure 4F,G), confirming PPAR $\gamma$  activation as a key step to execute metabolic remodeling during cAMP-induced adipocyte browning.

#### 3.5. Improved ATAC-seq method works effectively for adipocytes

To interrogate the regulatory mechanisms underlying the biphasic transcriptional response during FSK-induced adipocyte browning, we sought to determine changes in the chromatin landscape using ATAC-

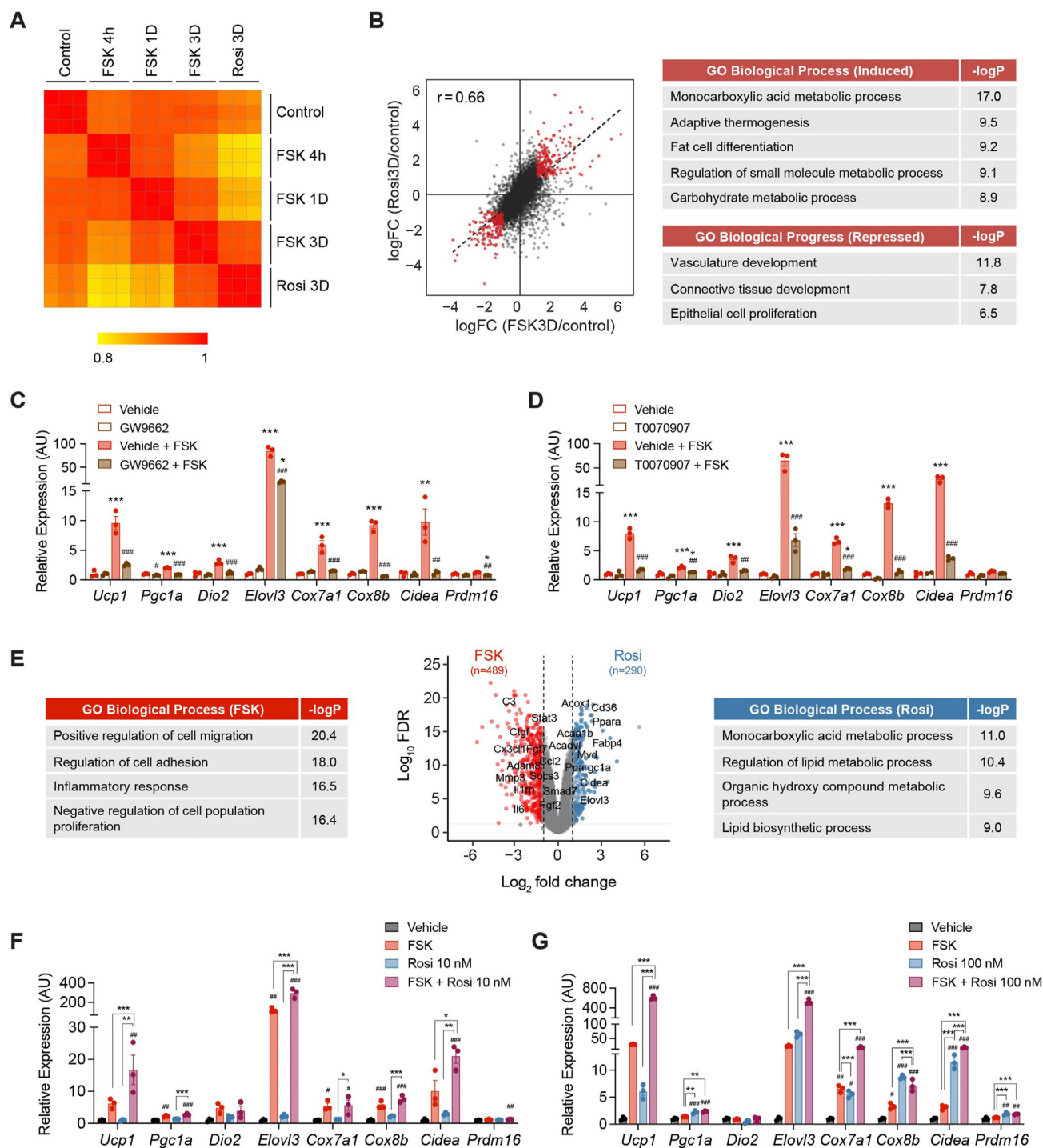


**Figure 4: Chronic FSK induces gene expression changes similar to, but distinct from Rosi treatment.** (A) Similarity matrix showing pairwise Pearson correlations between transcriptomic profiles of different samples. Pearson correlation coefficient  $r$  is presented in color as indicated. (B) Scatterplot showing correlation of fold changes of the differentially expressed genes (DEGs) upon chronic FSK versus Rosi treatment. The black dashed line indicates the trend line. Dots highlighted in red represent the genes significantly induced or repressed by both treatments in the same direction. Pathways (GO biological process) enriched in each set of genes and their  $-\log_{10}P$  values are presented in the table on the right. (C–D) Effects of PPAR $\gamma$  inhibitors GW9662 (10  $\mu$ M) (C) and T0070907 (10  $\mu$ M) (D) on thermogenic gene expression upon chronic FSK treatment for 3 days ( $n = 3$ ). (E) Volcano plot showing fold changes of gene expression in differentiated MAP adipocytes treated with FSK versus Rosi for 3 days. Each dot represents individual gene, highlighted if significantly upregulated by FSK (left) or by Rosi (right). Significance is determined by  $FDR < 0.05$  and  $|\log_2FC| > 1$ . Representative DEGs are labeled. Pathways (GO biological process) enriched in the FSK- (left) and Rosi-induced (right) genes and their  $-\log_{10}P$  values are shown in tables. (F–G) Effects of low concentrations of Rosi (10 nM (F) or 100 nM (G)) on the FSK-induced changes in thermogenic genes ( $n = 3$ ). Data are presented as mean  $\pm$  SEM. Statistical analysis was performed by two-way ANOVA with Tukey's post-hoc test (C–D) ( $*P < 0.05$ ;  $**P < 0.01$ ,  $***P < 0.001$  between vehicle vs. vehicle + FSK and  $\#P < 0.05$ ;  $\#\#P < 0.01$ ,  $\#\#\#P < 0.001$  between vehicle vs. GW9662 or vehicle + FSK vs. GW9662 + FSK) or one-way ANOVA with Tukey's post-hoc test (F–G) ( $*P < 0.05$ ;  $**P < 0.01$ ,  $***P < 0.001$  and  $\#P < 0.05$ ;  $\#\#P < 0.01$ ,  $\#\#\#P < 0.001$  relative to vehicle).

seq. While ATAC-seq is a simple but powerful method of assessing chromatin accessibility, it struggles with a high fraction of contaminating sequencing reads from mitochondrial DNA, ranging from 20% up to 90% of the total reads [42]. This problem can be exacerbated with certain cell types containing high mitochondrial contents such as adipocytes, liver and muscles. To overcome this challenge, we developed an advanced protocol for ATAC-seq using a nucleus sorting strategy to minimize mitochondrial contamination. From differentiated MAP cells collected, we isolated nuclei and subjected them to flow cytometry. High-quality single nucleus populations were sorted by gating based on size, complexity, and DNA contents (Figure 5A). We further optimized tagmentation and library generation steps for a lower nucleus number ( $n = 10,000$ ) using a reduced volume of tagmentation reagents (25  $\mu$ l) compared to the standard ATAC-seq protocol (see the Method section for details), thereby improving the sensitivity and cost-

effectiveness of the protocol. This method generated a well-defined pattern of nucleosomal periodicity (Figure S4A), which is one of the features of high-quality ATAC-seq libraries. In addition, we implemented a quality control (QC) step for the libraries using qPCR to determine the chromatin accessibility at multiple genomic loci. We designed primers that target low or high peaks present in adipose tissues as well as closed gene desert regions as background controls (Figure S4B). The qPCR analysis showed 7–25-fold and 25–80-fold enrichment at the low and high peaks, respectively, compared to the negative control background (Figure 5B), which is indicative of successful samples. Subsequent sequencing of the ATAC-seq libraries revealed a remarkable improvement in lowering the fraction of mitochondrial reads down to 3–6% of the total reads (Figure 5C) and in increasing the fraction of reads contributing to peaks up to 40–55% of the total reads (Figure 5D). Finally, we were able to identify multiple

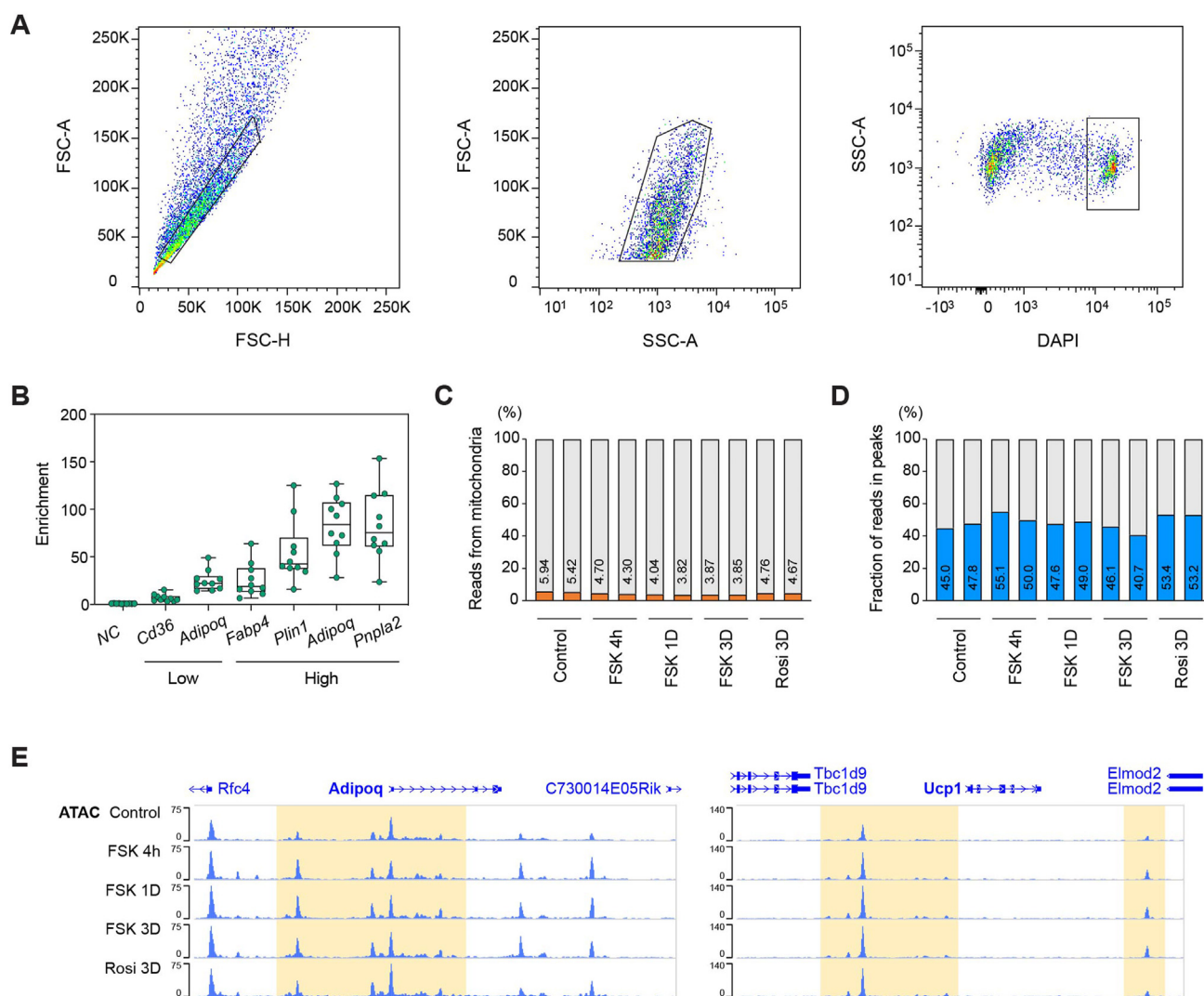


**Figure 5: Improved ATAC-seq methods works effectively for adipocytes.** (A) Gating strategy for sorting adipocyte nuclei. Isolated nuclei were incubated with Hoechst (1 ng/ml). During sorting, doublets were excluded by plotting the height against the area for forward scatter (FSC) (left). Then, within the gate (middle) inclusive of nuclei in various sizes and complexities based on the FSC and side scatter (SSC), only Hoechst-labeled population (right) was collected. (B) ATAC-PCR validation prior to sequencing using primers for adipocyte marker genes. Enrichment of the DNA fragments containing target sequence of each primer set was calculated against the negative control (NC). The intensity of ATAC peaks targeted by the primers is indicated as low or high. Bars indicate mean  $\pm$  SEM ( $n = 10$ ; duplicates per condition). See also Figure S4. (C–D) Quality check of ATAC-seq. The proportion of reads from mitochondria, which indicates mitochondrial DNA contamination (C), and the fraction of reads that fall into the called peak regions (D) across samples. (E) ATAC-seq signal tracks of representative samples (one per condition) at the general adipocyte marker *Adipoq* and the thermogenic marker *Ucp1*.

sharp ATAC-seq peaks with low noises at the loci of the adipocyte marker *Adipoq* and brown adipocyte marker *Ucp1* (Figure 5E). Altogether, our improved ATAC-seq protocol effectively works for adipocytes.

### 3.6. Chromatin accessibility exhibits different dynamics during cAMP-Induced browning

Using our new ATAC-seq protocol, we characterized how the chromatin accessibility landscape is altered in differentiated MAP cells in the course of biphasic FSK-induced browning in comparison with single-phase Rosi-induced browning. Strikingly, the PCA revealed divergent patterns of the chromatin dynamics occurring during FSK and Rosi treatments. The chromatin landscape was modified most dramatically after 4 h of FSK treatment and partly returned toward the control state later after 1 day and 3 days of the treatment (Figure 6A). These kinetics were quite distinct from the Rosi-driven change in the chromatin state. Rosi made a marginal change, moving the chromatin profile mostly along the PC2, which explains only 13.5% of the variance, while PC1 does more than 50% of the variance (Figure 6A). Consistently, a global pairwise correlation analysis found a clear segregation between FSK- and Rosi-treated adipocytes. Adipocytes treated with FSK for different periods showed similar chromatin profiles. However, they were markedly different from the profile of the Rosi-treated cells, which was rather close to the control adipocyte state (Figure 6B). Taken together, our work shows that, despite the similarity in their transcriptomic effects, FSK triggers a significant chromatin landscape remodeling process, whereas Rosi has minimal impact on chromatin.

To explicate the dynamics of the chromatin landscape during adipocyte browning, we conducted unbiased K-means clustering with the differentially regulated ATAC-seq peaks (Figure 6C), which identified 5 major peak clusters in a biphasic pattern of changes following FSK treatment. Peak Clusters 1 and 2/4 were closed and open, respectively, at the early phase after FSK treatment, whereas Peak Cluster 5 opened at the later phase. Peak Cluster 3 stayed closed throughout FSK treatment, but was opened by Rosi (Figure 6C). Unlike RNA-seq data, we found significant differences between the chromatin states shaped after 3 d FSK and Rosi treatments; specifically, the peaks included in Peak Clusters 2, 3 and 5 were affected in the opposite direction. Furthermore, the unbiased clustering failed to find peak clusters that were commonly opened by long-term FSK and Rosi treatments (Figure 6C), suggesting that the chromatin landscape dynamics are regulated in a discordant kinetics in comparison with the transcriptomic changes.

To find the mechanisms that coordinate chromatin accessibility and gene expression during the biphasic adipocyte browning, we first associated ATAC-seq peaks with nearby genes, categorized them by the gene clusters identified in the RNA-seq, and analyzed the patterns of their changes across conditions within each gene cluster using K-means clustering. We focused on the peaks associated with Gene Cluster 4 (early-induced genes) and Gene Cluster 5 (late-induced genes) since we looked for mechanisms that mediate the biphasic gene expression during FSK-induced adipocyte browning. Among the 3 clusters characterized from the peaks associated with Gene Cluster 4 (Figure S5A), Peak Cluster 1 (47% of the associated peaks) showed a consistent pattern with the changes in gene expression that was acutely induced specifically by FSK at the early phase but with the exception that chromatin stayed open until the late phase, where the gene expression was rapidly repressed back comparable to the control

state (Figures S5A and 6D). The transcription factor *Fos*, which has a key role in cAMP signaling during inflammation [43,44], was one of the examples of this Peak Cluster 1 (Figure 6D). The other Peak Cluster 2 or 3 displayed disagreeing patterns with the gene expression changes, as the peaks were opened also by Rosi or were altered in the exact opposite direction, respectively (Figure S5A). On the other hand, with the peaks associated with Gene Cluster 5, we found 4 clusters, none of which showed a matched pattern to the late induction of the genes (Figure S5B). The Gene Cluster 5-associated Peak Cluster 1, 3 and 4 exhibited completely inconsistent patterns, implying that these peaks may not have direct roles in the regulation of transcription (Figure S5B). By contrast, an interesting pattern was captured in the Gene Cluster 5-associated Peak Cluster 2, which occupies ~20% of the associated peaks. These peaks were opened by both FSK and Rosi, and specifically, responded to FSK starting from the early phase preceding transcriptional activation (Figures S5B and 6E). For example, the accessibility of the promoter regions of the thermogenic gene *Cox7a1* increased after 4 h of FSK treatment and stayed high while its gene expression was not induced until after 3 days of the treatment (Figure 6E). Taken together, chromatin landscape remodeling is not directly carried over to transcriptomic changes, and rather precedes or persists after transcriptional regulation. This may serve as a mechanism to achieve the smooth transition observed during the biphasic transcriptional responses.

### 3.7. NFIL3 plays an important role in cAMP-Induced adipocyte browning

We sought to identify transcription factors that drive the biphasic transition during FSK-induced adipocyte browning. To this end, employing motif discovery approaches, we computationally searched for candidate transcription factors (TFs) that potentially bind to the DNA elements over-represented in the peaks of our interest. From the early-induced Gene Cluster 4-associated Peak Cluster 1, the transcription factor families of FOS/JUN, CEBP/NFIL3, ATF and TEAD, which are known to control inflammation [43,44], cell morphology [45–47] and migration [48,49] via cAMP signaling, were found to be enriched (Figure S6A). Intriguingly, we found that the late-induced Gene Cluster 5-associated Peak Cluster 2 were also enriched with the transcription factor motifs of FOS/JUN and CEBP/NFIL3 as in the Gene Cluster 4-associated Peak Cluster 1. On the other hand, PPAR $\gamma$  motifs were specifically enriched in this late-induced peak cluster (Figure S6B). This corroborates the finding from RNA-seq data that PPAR $\gamma$  is a key TF directing thermogenic gene expression program during the late phase of FSK-induced adipocyte browning. We also noted that CCCTC-Binding Factor (CTCF), a regulator of chromatin conformation, appears in the list (Figure S6B), suggesting its active role in chromatin remodeling during adipocyte browning.

We hypothesized that the TFs enriched in both early- and late-phase peak clusters, such as FOS/JUN and CEBP/NFIL3, may play an important role in transitioning between the phases during the browning response. FOS/JUN is a well-known player in inflammatory signaling [43,44,50], and CEBP $\beta$  has been reported to promote a cell fate switch from myoblastic progenitors to brown adipocytes by interacting with PRDM16, a transcriptional coregulator [51]. Therefore, we explored a potential function of NFIL3, which remains uncharacterized, especially in the context of adipocyte browning. The known NFIL3 motif was significantly matched with a *de novo* motif identified from the early- and late-phase peak clusters (Figure 7A). We first assessed *Nfil3* mRNA expression in the course of time following FSK treatment up to

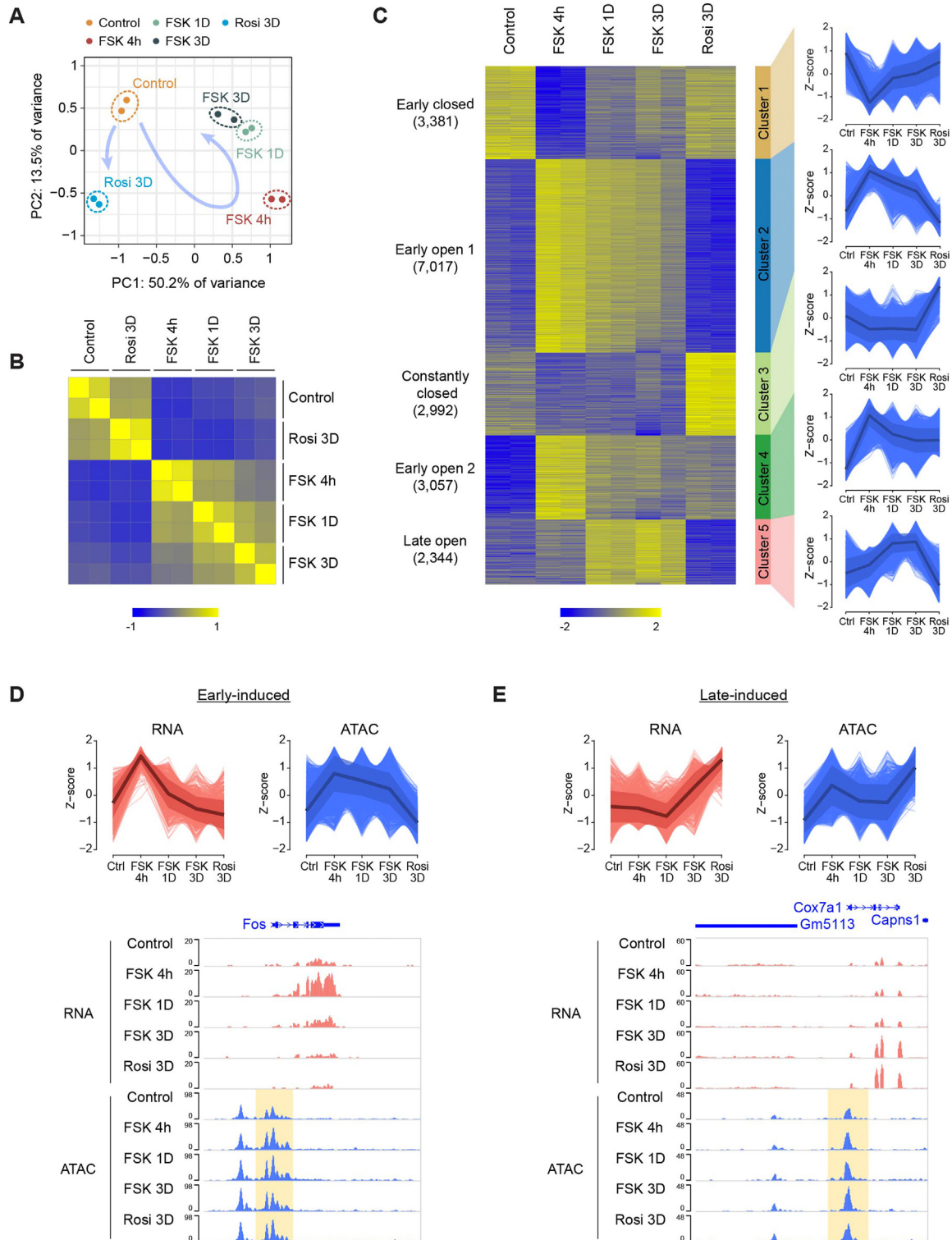


**Figure 6: Chromatin accessibility dynamics during FSK-induced cAMP stimulation exhibits different kinetics from that of transcriptomic profiles. (A)** PCA of ATAC-seq data from differentiated MAP cells treated with FSK or Rosi. Each dot indicates an individual replicate ( $n = 2$ ). **(B)** Similarity matrix showing pairwise Pearson correlation between samples based on the profiles of differentially regulated ATAC peaks. Total number of differentially regulated peaks is 18,791. Pearson correlation coefficient  $r$  is presented in color as indicated. **(C)** Heatmap of relative intensity (Z-score) of differentially regulated ATAC peaks (rows) across samples (columns). Peaks are classified into 5 clusters by K-means clustering based on their patterns as labeled. Parallel coordinate plot on the right shows the Z-score trends of individual ATAC peaks across conditions in each cluster. The black solid line and the ribbon indicate mean and SD, respectively. **(D–E)** Distinct patterns of gene expression versus chromatin accessibility upon treatment with FSK or Rosi. Parallel coordinate plots of relative gene expression (left) and ATAC peak intensity (right) for the early-induced genes (D) and for the late-induced genes (E). RNA- and ATAC-seq signal tracks at the loci of representative genes *Fos* (D) and *Cox7a1* (E) throughout the treatment conditions, with ATAC-seq signals highlighted. See also Figure 5.

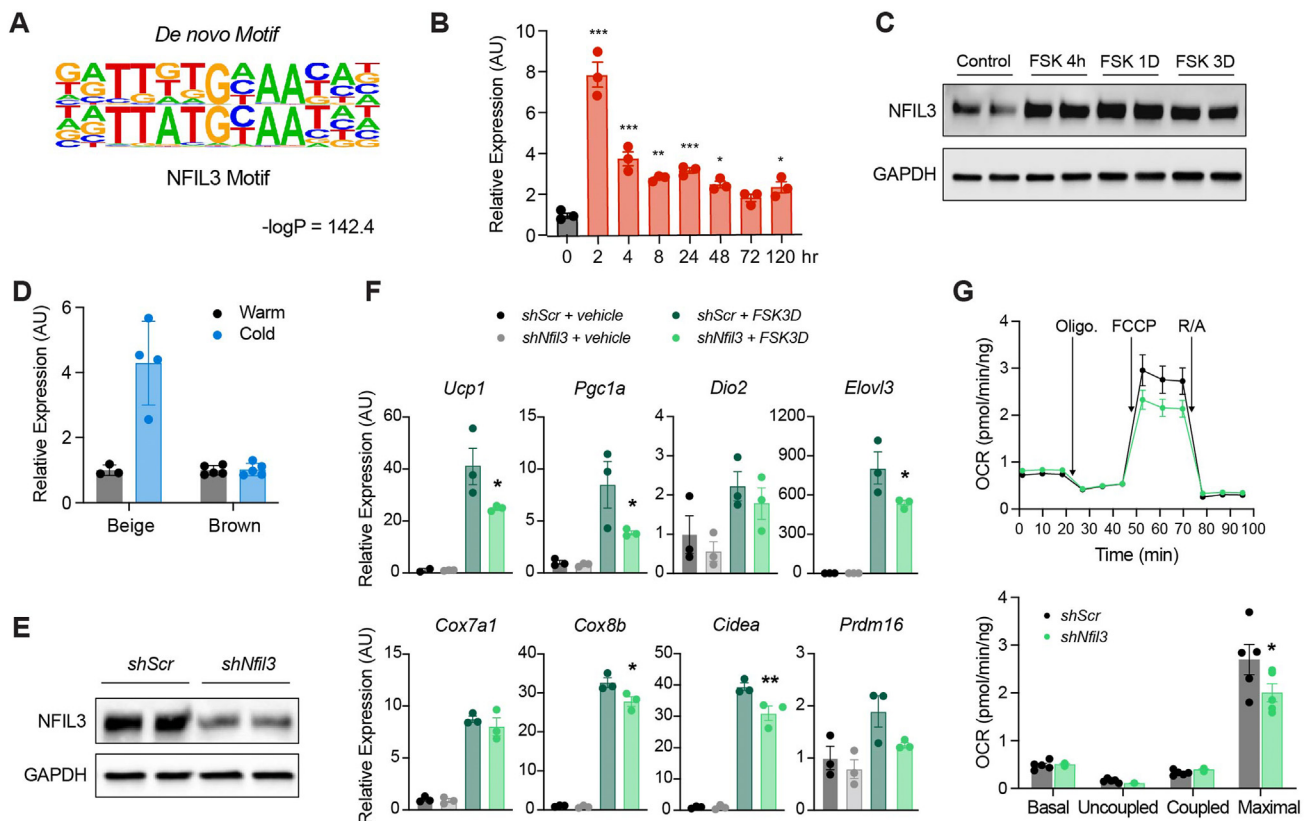


**Figure 7: NFIL3 is important for cAMP induced adipocyte browning.** (A) Binding sequence position weight matrix (PWM) of NFIL3 motif, generated by *de novo* motif analysis using Homer (B) Expression of *Nfil3* at baseline and at the indicated time points after treatment with FSK (10  $\mu$ M) ( $n = 3$ ). (C) Protein levels of NFIL3 in response to FSK at baseline and at the indicated time points. GAPDH was used as a loading control ( $n = 2$ ). (D) Expression of *Nfil3* in beige and brown adipocytes from warm and cold temperature. (E) Protein levels of NFIL3 in differentiated MAP cells infected with lentivirus expressing shRNA against with scramble (*shScr*) or *Nfil3* (*shNfil3*). GAPDH was used as a loading control ( $n = 2$ ). (F) Expression of thermogenic genes after FSK treatment for 3 days in differentiated MAP cells infected with *shScr* and *shNfil3* ( $n = 3$ ). (G) OCR in differentiated MAP cells infected with *shScr* and *shNfil3* ( $n = 5$ ). Bar graphs represent the quantification of basal, uncoupled, coupled, and maximal mitochondrial respiration. Data are presented as mean  $\pm$  SEM. Statistical analysis was performed by one-way ANOVA with Dunnett's post-hoc test (B) ( $*P < 0.05$ ;  $**P < 0.01$ ;  $***P < 0.001$  relative to time 0) or with Sidak's post-hoc test (F) ( $*P < 0.05$ ;  $**P < 0.01$  relative to *shScr*), two-sided Student's *t*-test ( $*P < 0.05$ ), or two-way ANOVA with Tukey's post-hoc test (G) ( $*P < 0.05$ ).

120 h. Its gene expression level was significantly induced as early as 2 h after the treatment and reduced thereafter but stayed higher than the control throughout the browning process (Figure 7B). Similarly, the NFIL3 protein level was induced as early as 4 h and remained more abundant until 3 days after the treatment (Figure 7C). Next, we further analyzed our previous RNA-seq data of brown and beige adipocytes [5] and found that *Nfil3* was induced by cold temperature in iWAT, but not in BAT (Figure 7D). This suggests that NFIL3 is specifically involved in the recruitment of beige adipocytes not classical brown adipocytes. When *Nfil3* was knocked down in differentiated MAP cells using lentivirus-mediated shRNA (Figure 7E), expression of most thermogenic genes was significantly reduced after 3 d FSK treatment but not after 4 h treatment (Figure 7F and Figure S7A). This indicates that NFIL3 is essential for induction of the 2nd phase of cAMP-driven adipocyte browning. Consistently, mitochondrial maximal oxygen consumption rate was also significantly inhibited by *shNfil3* during 3 d FSK treatment (Figure 7G,H), providing evidence of a lower mitochondrial respiration capacity resulted from reduced NFIL3 expression. Importantly, *shNfil3* did not significantly affect thermogenic gene expression during 3 d Rosi treatment (Figure S7B), indicating that NFIL3 functions specifically for cAMP-induced biphasic responses. Taken together, these results suggest that NFIL3 is an important mediator of the biphasic cAMP-induced adipocyte browning.

#### 4. DISCUSSION

Inducible thermogenic brown adipocytes have been suggested as a new target for the treatment of obesity and related metabolic disease, including type 2 diabetes [11–13,52]. One example of promising target molecules is  $\beta$ 3-AR, which has been demonstrated to promote the browning of adipose tissue through a robust cAMP activation and, in turn, protect against obesity and associated metabolic dysfunction in rodent studies [53,54]. However, the use of  $\beta$ 3-AR agonists has not been clinically proven to be effective in humans and is accompanied by side effects, such as tachycardia and hypertension [55]. Rosi is a potent browning agent and insulin sensitizer working by activating PPAR $\gamma$ , a master regulator of lipid metabolism. However, some adverse effects, including weight gain, edema and heart failure can also occur [56,57]. Currently, the limited efficacy of pharmacological drugs has necessitated further studies on molecular mechanisms by which the adipocyte browning process is induced and regulated by various types of different stimuli. In this study, using a new adipocyte cell line developed to possess a higher thermogenic potential, we comprehensively characterized transcriptomic and epigenomic changes during adipocyte browning induced by the activation of cAMP (FSK) and PPAR $\gamma$  (Rosi). Here, we employed an improved protocol for chromatin accessibility assays for a higher quality. The current study

revealed similarities and differences in the browning process triggered by FSK and Rosi based on the time-course analysis and identified NFIL3 as a new regulator of adipocyte browning.

We first sought an *in vitro* cell model system as a replacement for current cell models to better achieve adipocyte browning. Though 3T3L1 cells are the most widely used in adipose biology, our results demonstrated that their thermogenic gene expression is minimal at the basal state and not robustly induced, even upon stimulation by browning agents. In particular, the most well-known browning marker *Ucp1* was not inducible at all. This is not surprising considering that 3T3L1 cells originate from mouse embryonic fibroblasts. 3T3L1 cells rather represent a cell model for white adipocytes like other 3T3-derived cell lines including 3T3-F442A [58]. Immortalized mouse brown adipocyte cell lines, including BAT1 [59] and iBA [60], have been used to study adipocyte thermogenesis. However, given their origins in interscapular BAT, it is unclear whether they can exhibit cellular plasticity as beige adipocytes have. By contrast, MAP cells we created have a higher thermogenic gene expression and respond to browning stimuli more vigorously in comparison with 3T3L1 cells. Importantly, MAP cells retain the expression of marker genes of *in vivo* iWAT, such as *Shox2*, *Tbx1*, and *Hoxc9*. This is a significant improvement, as these markers play a key role in exerting beige adipocyte functions. For example, TBX1 has been shown to control adipose thermogenic capacity *in vivo* [61] and represent the most accurate marker of beige adipocytes [5]. Indeed, upon chronic treatment with FSK or Rosi, MAP cells displayed similar transcriptomic changes to those occurring in beige adipocytes *in vivo* during cold exposure, ensuring that they are a new useful cell model for the study of beige adipocyte development.

Time-course transcriptomic analysis revealed distinct trajectories of the browning process in MAP cells following FSK and Rosi treatments. Rosi slowly, but directly, induced gene expression for thermogenesis and lipid metabolism, whereas FSK prompted a highly dynamic biphasic response. The first early phase within 24 h of FSK treatment involves stimulation of inflammatory signaling, cytoskeletal organization and vascularization. This is consistent with the previous reports that adipose browning is accompanied by substantial tissue remodeling processes initiated by coordinated actions of multiple cell types, including immune, endothelial and smooth muscle cells [62]. It remains to be determined how the gene expression changes can be reflected in cellular functionality. The later phase, commencing after 3 days of cAMP stimulation, was characterized by full-scale activation of thermogenesis and cellular metabolism. It is in line with the fact that beige adipocytes require at least 3 days to appear in iWAT during cold exposure [21]. Intriguingly, we observed similar biphasic gene expression responses in iWAT of mice exposed to cold temperature for 3 days, suggesting that FSK better mimics *in vivo* adipose browning. Despite following different trajectories during 3 days of stimulation, both Rosi and FSK drove adipocytes to similar cellular states, to a greater extent. Given that FSK affects a broad range of downstream targets of cAMP signaling, unlike Rosi, which directly affects PPAR $\gamma$  activation, the biphasic FSK response may lead to PPAR $\gamma$  activation of functional thermogenesis. Indeed, we demonstrated that PPAR $\gamma$  is indispensable to cAMP activation-derived thermogenesis by abrogating its thermogenic gene induction with PPAR $\gamma$  inhibitors. Consistently, the presence of minimal amounts of Rosi during 3 d FSK treatment synergistically augmented the thermogenic gene expression of MAP cells. However, our comparison of transcriptomic profiles between FSK- and Rosi-treated MAP cells helped to identify their distinct features, particularly in cell migration/adhesion and inflammatory-related processes, uncovering some

functional differences of beige adipocytes determined by different environmental cues. This can be explained by cellular heterogeneity shaped within brown and/or beige adipocyte population. A recent single-nucleus RNA-seq of mouse interscapular BAT has discovered a rare subpopulation of brown adipocytes executing anti-thermoregulatory functions [63]. Long-term cold exposure generates a unique type of beige adipocytes from a myogenic lineage in BAT, which serves a critical role in cold adaptation with enhanced glycolytic activity as a non-canonical mechanism [64]. In this context, different browning agents may recruit slightly distinct beige adipocyte subpopulations. Like our study, it has been reported that different browning stimuli CL-316,243, Rosi, and roscovitine give rise to discrete populations of UCP1-expressing adipocytes in iWAT, which display distinct gene expression profiles [65]. As suggested in this study, the functional heterogeneity of brown/beige adipocytes in response to diverse physiological and pathological conditions remains to be characterized by future studies.

Not limited to the transcription-level responses, we further interrogated chromatin remodeling occurring during adipocyte browning upon FSK and Rosi treatments. We revised the ATAC-seq protocol for a quality improvement by adding several important features. First, the removal of mitochondria and other contaminating cell and tissue debris by nucleus sorting enables the generation of high-quality data. This not only prevents the wasting sequencing reads coming from contaminating mitochondria but also minimizes the variations between different batches and experiments. Second, this protocol scales down the reaction volume optimized for low inputs. It curtails the cost of experiments, as well as sorting time. Lastly, the additional qPCR-based QC step can determine sample quality before sequencing. Unlike chromatin immunoprecipitation (ChIP) assays, that are often checked by qPCR before sequencing, such methods have not been used for chromatin accessibility assays, possibly because the sequencing libraries are directly produced without a break point in-between and no solid method to quantify chromatin accessibility by qPCR exists. Here, we performed qPCR directly on ATAC-seq libraries, so called ATAC-PCR, using primers designed to target some previously defined genomic regions. The primers include the ones targeting closed gene-free regions for background controls and others targeting open chromatin regions near adipocyte marker genes for positive controls. We used 2 types of primers for positive controls, low and high peak-targeting primers, which enabled us to measure the sensitivity of the assays. Our ATAC-seq samples, shown to be substantially enriched at the peaks of adipocyte marker genes in the QC qPCR step, indeed produced high quality data after sequencing and analysis. By applying the steps of high-quality nucleus isolation, this ATAC-seq protocol can be applied to any cell or tissue type, including tissues that prove difficult to be homogenized or contain a great deal of debris, such as skeletal muscle and bone. The QC qPCR step requires prior knowledge of the closed and open genomic regions specifically in the target cell types, but for uncharacterized cell types, universal negative and positive primer sets for ubiquitously closed and open genomic regions, respectively, can be used. Our protocol will potentially facilitate the application of ATAC-seq to diverse biological samples with minimum trial-and-error.

To our surprise, the ATAC-seq data revealed the distinct impacts of FSK and Rosi treatments on the chromatin landscape, despite the comparable transcriptomic profiles they created in 3 days. In contrast to Rosi producing minimal changes, FSK led to drastic biphasic chromatin remodeling, where the chromatin landscape changed at the early phase within 4 h and was gradually restored to its original state during the late phase. Our findings demonstrate that the

mechanisms of transcriptional regulation by Rosi are independent of chromatin rearrangements or involve a minimum of them. Rosi is known to promote the binding of PPAR $\gamma$  to target genes by recruiting cofactors, such as MED1, p300, and CBP, for transcriptional activation [66,67]. However, its effects on chromatin states remain largely unknown. The differential impact on chromatin structures versus transcriptional regulation have also shown in estradiol, a ligand of the estrogen receptor, which induces modest changes in chromatin accessibility but exerts a broad effect on gene expression [68]. These findings suggest that ligand-mediated gene regulation via nuclear hormone receptors may not require a global chromatin remodeling process. It is also possible that other types of epigenetic mechanisms, such as histone modification and DNA methylation, govern the PPAR $\gamma$ -mediated gene regulation and therefore needs to be determined in the future. On the other hand, with the integration of RNA-seq and ATAC-seq data, we unexpectedly observed that the biphasic chromatin remodeling by FSK treatment displays different kinetics compared to the transcriptional regulation of corresponding genes. The early-induced genes were associated with ‘lingering’ chromatin regions that open acutely upon FSK stimulation and stay open until the late phase, while the gene expression shuts off again. Conversely, the late-induced genes contain ‘preceding’ chromatin regions that open ahead of the transcriptional activation at the early phase. These observations demonstrate that chromatin accessibility alone is not a sufficient determinant of gene expression during cAMP-induced adipocyte browning requiring additional epigenetic mechanisms for precise control. Such discordant kinetics of the chromatin landscape during *in vivo* adipose tissue browning during cold acclimation should be further investigated. However, considering that the epigenetic memory of cold adaptation is retained as poised enhancer histone marks in re-warmed beige adipocytes for an accelerated response in the future cold exposure [5], the preceding or persisting chromatin accessibility changes may function as a mechanism of priming gene expression upon recurrent stimulation. Lastly, applying motif discovery methods to the ATAC-seq peaks annotated to the early- and late-induced genes, we propose NFIL3 as a new TF regulating the biphasic cAMP-induced adipocyte browning. NFIL3, also known as E4 promoter-binding protein 4 (E4BP4), is a basic leucine zipper (b-ZIP) TF that has been shown to control circadian rhythm [69], immunity [70], and cancer [71]. Its role in metabolic regulation has started to be reported in various tissues. In the liver, NFIL3 controls lipogenesis, bile acid and xenobiotic metabolism, and glucose homeostasis [72–75]. In the intestine, in response to microbiota-derived immune signaling, NFIL3 controls the expression of genes involved in circadian lipid metabolism and systemic nutrient homeostasis [76]. Though the role of NFIL3 in adipose tissues has not yet been established, a recent study demonstrated that NFIL3 contributes to adipose tissue inflammation during obesity by maintaining the function of adipose natural killer cells [77]. Our data provides new evidence that NFIL3 directly acts on adipocytes affecting their metabolism. The observation that NFIL3 binding motif was enriched in both groups of peaks assigned to early- and late-induced genes is in line with the expression of NFIL3 itself, at mRNA and protein levels. This started increasing instantly after cAMP activation and stayed relatively high during the entire adipocyte browning for 3 days. These results are in line with a previous report of NFIL3 as a candidate transcriptional regulator of short-term norepinephrine stimulation in adipocytes [78]. Interestingly, *Nfil3* knockdown by *shNfil3* led to reduced thermogenic gene expression, as well as cellular respiration only during chronic, but not acute, cAMP activation. The reduced maximal respiration with

unaffected uncoupled respiration by *shNfil3* suggests that NFIL3 may mediate cellular reprogramming for a full-scale adipocyte browning including mitochondrial biogenesis rather than directly promoting mitochondrial uncoupling. Motif analysis predicted that NFIL3 binding sites co-occur, not overlapping, with PPAR $\gamma$  sites in a set of the late-induced ATAC-seq peaks (data not shown). This suggests that NFIL3 may work in a complex with PPAR $\gamma$  for thermogenic gene induction during the late stage of adipocyte browning, although this potential mechanism remains to be examined. Importantly, recent genome-wide association studies (GWAS) reporting multiple single nucleotide polymorphisms (SNPs) near the *Nfil3* locus that are associated with body mass index (BMI) and visceral adiposity [79,80] corroborate the potential role of NFIL3 in human obesity and metabolic disease. Its specific functionalities in adipose thermogenesis and systemic energy homeostasis should be further confirmed by adipocyte-specific loss-of-function mutations of *Nfil3* using mouse models and/or human adipocyte cell models.

In conclusion, due to a new cell culture model and an advanced chromatin profiling method, we elucidated comprehensive changes in the transcriptome and chromatin accessibility of adipocytes in response to different browning agents, and therefore, proposed a new molecule mediating the biphasic browning response.

#### AUTHOR CONTRIBUTIONS

H.C.R. and J.S. conceived, designed and supervised the study. J.S., S.T., J.W., O.S., K.K. and H.C.R. performed experiments and interpreted the data. J.S. led computational data analysis under supervision of H.C.R., J.S. and H.C.R. wrote the manuscript with inputs from all the other authors. All authors read and approved the manuscript.

#### FUNDING

This study was supported by IUSM Showalter Research Trust Fund, IUSM Center for Diabetes and Metabolic Diseases Pilot and Feasibility grant, National Institute of Diabetes and Digestive and Kidney Diseases (R01DK129289), and American Diabetes Association Junior Faculty Award (7-21-JDF-056) to H.C.R.

#### ACKNOWLEDGEMENTS

We thank Dr. Charlie Dong for sharing equipment and Dr. Christina Santangelo for providing help with revising and proofreading the manuscript. We acknowledge the support from the Flow Cytometry Core and the Center for Medical Genomics at Indiana University School of Medicine.

#### CONFLICT OF INTEREST

None declared.

#### DATA AVAILABILITY

The raw and processed data of the RNA-seq and ATAC-seq in this paper are available in the Gene Expression Omnibus (GEO) repository.

#### APPENDIX A. SUPPLEMENTARY DATA

Supplementary data to this article can be found online at <https://doi.org/10.1016/j.molmet.2022.101619>.

## REFERENCES

- [1] Health, World. Organization., n.d. Obesity and overweight. <https://www.who.int/news-room/fact-sheets/detail/obesity-and-overweight>.
- [2] Must, A., Spadano, J., Coakley, E.H., Field, A.E., Colditz, G., Dietz, W.H., 1999. The disease burden associated with overweight and obesity. *JAMA* 282(16): 1523–1529. <https://doi.org/10.1001/JAMA.282.16.1523>.
- [3] Wu, J., Boström, P., Sparks, L.M., Ye, L., Choi, J.H., Giang, A.H., et al., 2012. Beige adipocytes are a distinct type of thermogenic fat cell in mouse and human. *Cell* 150(2):366–376. <https://doi.org/10.1016/J.CELL.2012.05.016>.
- [4] Cui, X., Nguyen, N.L.T., Zarebidaki, E., Cao, Q., Li, F., Zha, L., et al., 2016. Thermoneutrality decreases thermogenic program and promotes adiposity in high-fat diet-fed mice. *Physiological Reports* 4(10). <https://doi.org/10.14814/PHY2.12799>.
- [5] Roh, H.C., Tsai, L.T.Y., Shao, M., Tenen, D., Shen, Y., Kumari, M., et al., 2018. Warming induces significant reprogramming of beige, but not brown, adipocyte cellular identity. *Cell Metabol* 27(5):1121–1137. <https://doi.org/10.1016/j.cmet.2018.03.005> e5.
- [6] Heaton, J.M., 1972. The distribution of brown adipose tissue in the human. *J Anat* 112(Pt 1):35.
- [7] Lidell, M.E., Betz, M.J., Leinhard, O.D., Hegliind, M., Elander, L., Slawik, M., et al., 2013. Evidence for two types of brown adipose tissue in humans. *Nat Med* 19(5):631–634. <https://doi.org/10.1038/NM.3017>.
- [8] Kern, P.A., Finlin, B.S., Zhu, B., Rasouli, N., McGehee, R.E., Westgate, P.M., et al., 2014. The effects of temperature and seasons on subcutaneous white adipose tissue in humans: evidence for thermogenic gene induction. *J Clin Endocrinol Metab* 99(12):E2772–E2779. <https://doi.org/10.1210/JC.2014-2440>.
- [9] Jespersen, N.Z., Larsen, T.J., Peijs, L., Daugaard, S., Homøe, P., Loft, A., et al., 2013. A classical brown adipose tissue mrna signature partly overlaps with brite in the supraclavicular region of adult humans. *Cell Metabol* 17(5): 798–805. <https://doi.org/10.1016/j.cmet.2013.04.011>.
- [10] Cypess, A.M., White, A.P., Vnochet, C., Schulz, T.J., Xue, R., Sass, C.A., et al., 2013. Anatomical localization, gene expression profiling and functional characterization of adult human neck brown fat. *Nat Med* 19(5):635–639. <https://doi.org/10.1038/nm.3112>, 19:5.
- [11] Hanssen, M.J.W., Wierts, R., Hoeks, J., Gemmink, A., Brans, B., Mottaghy, F.M., et al., 2015. Glucose uptake in human brown adipose tissue is impaired upon fasting-induced insulin resistance. *Diabetologia* 58(3):586–595. <https://doi.org/10.1007/S00125-014-3465-8>.
- [12] Lee, P., Bova, R., Schofield, L., Bryant, W., Dieckmann, W., Slattery, A., et al., 2016. Brown adipose tissue exhibits a glucose-responsive thermogenic biorhythm in humans. *Cell Metabol* 23(4):602–609. <https://doi.org/10.1016/J.CMET.2016.02.007>.
- [13] Leitner, B.P., Huang, S., Brychta, R.J., Duckworth, C.J., Baskin, A.S., McGehee, S., et al., 2017. Mapping of human brown adipose tissue in lean and obese young men. *Proc Natl Acad Sci U S A* 114(32):8649–8654. <https://doi.org/10.1073/PNAS.1705287114>.
- [14] Chechi, K., Carpentier, A.C., Richard, D., 2013. Understanding the brown adipocyte as a contributor to energy homeostasis. *Trends Endocrinol Metabol: TEM (Trends Endocrinol Metab)* 24(8):408–420. <https://doi.org/10.1016/J.TEM.2013.04.002>.
- [15] Cao, W., Medvedev, A.V., Daniel, K.W., Collins, S., 2001.  $\beta$ -Adrenergic activation of p38 MAP kinase in adipocytes: cAMP induction of the uncoupling protein (UCP1) gene requires p38 MAP kinase. *J Biol Chem* 276(29):27077–27082. <https://doi.org/10.1074/JBC.M101049200>.
- [16] Lowell, B.B., Spiegelman, B.M., 2000. Towards a molecular understanding of adaptive thermogenesis. *Nature* 404(6778):652–660. <https://doi.org/10.1038/35007527>, 404:6778.
- [17] Dempersmier, J., Sambeat, A., Gulyaeva, O., Paul, S.M., Hudak, C.S.S., Raposo, H.F., et al., 2015. Cold-inducible Zfp516 activates UCP1 transcription to promote browning of white fat and development of brown fat. *Mol Cell* 57(2):235–246. <https://doi.org/10.1016/J.MOLCEL.2014.12.005>.
- [18] Scarpace, P.J., Matheny, M., 1996. Thermogenesis in brown adipose tissue with age: post-receptor activation by forskolin. *Pflug Arch Eur J Physiol* 431(3):388–394. <https://doi.org/10.1007/BF02207276>.
- [19] Mirbolloki, M.R., Upadhyay, S.K., Constantinescu, C.C., Pan, M.L., Mukherjee, J., 2014. Adrenergic pathway activation enhances brown adipose tissue metabolism: a [ $^{18}$ F]FDG PET/CT study in mice. *Nucl Med Biol* 41(1):10–16. <https://doi.org/10.1016/J.NUCMEDBIO.2013.08.009>.
- [20] Ohno, H., Shinoda, K., Spiegelman, B.M., Kajimura, S., 2012. PPAR $\gamma$  agonists induce a white-to-brown fat conversion through stabilization of PRDM16 protein. *Cell Metabol* 15(3):395–404. <https://doi.org/10.1016/J.CMET.2012.01.019>.
- [21] Wang, Q.A., Tao, C., Gupta, R.K., Scherer, P.E., 2013. Tracking adipogenesis during white adipose tissue development, expansion and regeneration. *Nat Med* 19(10):1338–1344. <https://doi.org/10.1038/nm.3324>.
- [22] van der Lans, A.A.J.J., Hoeks, J., Brans, B., Vijgen, G.H.E.J., Visser, M.G.W., Vosselman, M.J., et al., 2013. Cold acclimation recruits human brown fat and increases nonshivering thermogenesis. *J Clin Investig* 123(8):3395–3403. <https://doi.org/10.1172/JCI68993>.
- [23] Rosenwald, M., Perdikari, A., Rüllicke, T., Wolfrum, C., 2013. Bi-directional interconversion of brite and white adipocytes. *Nat Cell Biol* 15(6):659–667. <https://doi.org/10.1038/NCB2740>.
- [24] Roh, H.C., Tsai, L.T.Y., Lyubetskaya, A., Tenen, D., Kumari, M., Rosen, E.D., 2017. Simultaneous transcriptional and epigenomic profiling from specific cell types within heterogeneous tissues in vivo. *Cell Rep* 18(4):1048–1061. <https://doi.org/10.1016/j.celrep.2016.12.087>.
- [25] Chen, S., Zhou, Y., Chen, Y., Gu, J., 2018. fastp: an ultra-fast all-in-one FASTQ preprocessor. *Bioinformatics* 34(17):i884–i890. <https://doi.org/10.1093/BIOINFORMATICS/BTY560>.
- [26] Dobin, A., Davis, C.A., Schlesinger, F., Drenkow, J., Zaleski, C., Jha, S., et al., 2013. STAR: ultrafast universal RNA-seq aligner. *Bioinformatics* 29(1):15–21. <https://doi.org/10.1093/BIOINFORMATICS/BTS635>.
- [27] Liao, Y., Smyth, G.K., Shi, W., 2014. featureCounts: an efficient general purpose program for assigning sequence reads to genomic features. *Bioinformatics* 30(7):923–930. <https://doi.org/10.1093/BIOINFORMATICS/BTT656>.
- [28] Robinson, M.D., McCarthy, D.J., Smyth, G.K., 2010. edgeR: a Bioconductor package for differential expression analysis of digital gene expression data. *Bioinformatics* 26(1):139–140. <https://doi.org/10.1093/BIOINFORMATICS/BTP616>.
- [29] Zhou, Y., Zhou, B., Pache, L., Chang, M., Khodabakhshi, A.H., Tanaseichuk, O., et al., 2019. Metascape provides a biologist-oriented resource for the analysis of systems-level datasets. *Nat Commun* 10(1). <https://doi.org/10.1038/S41467-019-09234-6>.
- [30] Blighe, K., Rana, S., Lewis, M., 2021. EnhancedVolcano: publication-ready volcano plots with enhanced colouring and labeling.
- [31] Chen, S., Zhou, Y., Chen, Y., Gu, J., 2018. fastp: an ultra-fast all-in-one FASTQ preprocessor. *Bioinformatics* 34(17):i884–i890. <https://doi.org/10.1093/BIOINFORMATICS/BTY560>.
- [32] Langmead, B., Salzberg, S.L., 2012. Fast gapped-read alignment with Bowtie 2. *Nat Methods* 9(4):357–359. <https://doi.org/10.1038/nmeth.1923>, 9:4.
- [33] Li, H., Handsaker, B., Wysoker, A., Fennell, T., Ruan, J., Homer, N., et al., 2009. The sequence alignment/map format and SAMtools. *Bioinformatics* 25(16):2078–2079. <https://doi.org/10.1093/BIOINFORMATICS/BTP352>.
- [34] Zhang, Y., Liu, T., Meyer, C.A., Eeckhoute, J., Johnson, D.S., Bernstein, B.E., et al., 2008. Model-based analysis of ChIP-seq (MACS). *Genome Biol* 9(9):1–9. <https://doi.org/10.1186/GB-2008-9-9-R137/FIGURES/3>.

- [35] Zhou, X., Wang, T., 2012. Using the wash U Epigenome browser to examine genome-wide sequencing data. *Current Protocols in Bioinformatics* 40(1). <https://doi.org/10.1002/0471250953.BI1010S40>, 10.10.1-10.10.14.
- [36] Quinlan, A.R., Hall, I.M., 2010. BEDTools: a flexible suite of utilities for comparing genomic features. *Bioinformatics* 26(6):841–842. <https://doi.org/10.1093/BIOINFORMATICS/BTQ033>.
- [37] Kent, W.J., Zweig, A.S., Barber, G., Hinrichs, A.S., Karolchik, D., 2010. BigWig and BigBed: enabling browsing of large distributed datasets. *Bioinformatics* 26(17):2204–2207. <https://doi.org/10.1093/BIOINFORMATICS/BTQ351>.
- [38] Heinz, S., Benner, C., Spann, N., Bertolino, E., Lin, Y.C., Laslo, P., et al., 2010. Simple combinations of lineage-determining transcription factors prime cis-regulatory elements required for macrophage and B cell identities. *Mol Cell* 38(4):576–589. <https://doi.org/10.1016/J.MOLCEL.2010.05.004>.
- [39] Watanabe, M., Inukai, K., Katagiri, H., Awata, T., Oka, Y., Katayama, S., 2003. Regulation of PPAR $\gamma$  transcriptional activity in 3T3-L1 adipocytes. *Biochem Biophys Res Commun* 300(2):429–436. [https://doi.org/10.1016/S0006-291X\(02\)02860-7](https://doi.org/10.1016/S0006-291X(02)02860-7).
- [40] Lin, J.Z., Farmer, S.R., 2016. Morphogenetics in brown, beige and white fat development. *Adipocyte* 5(2):130. <https://doi.org/10.1080/21623945.2016.1140708>.
- [41] Tharp, K.M., Kang, M.S., Timblin, G.A., Saijo, K., Kumar, S., Stahl Correspondence, A., 2018. Actomyosin-mediated tension orchestrates uncoupled respiration in adipose tissues. *Cell Metabol* 27:602–615. <https://doi.org/10.1016/j.cmet.2018.02.005>.
- [42] Buenostro, J.D., Giresi, P.G., Zaba, L.C., Chang, H.Y., Greenleaf, W.J., 2013. Transposition of native chromatin for fast and sensitive epigenome profiling of open chromatin, DNA-binding proteins and nucleosome position. *Nat Methods* 10(12):1213–1218. <https://doi.org/10.1038/NMETH.2688>.
- [43] Koga, K., Takaesu, G., Yoshida, R., Nakaya, M., Kobayashi, T., Kinjyo, I., et al., 2009. Cyclic adenosine monophosphate suppresses the transcription of proinflammatory cytokines via the phosphorylated c-fos protein. *Immunity* 30(3):372–383. <https://doi.org/10.1016/J.IMMUNI.2008.12.021>.
- [44] Wen, A.Y., Sakamoto, K.M., Miller, L.S., 2010. The role of the transcription factor CREB in immune function. *J Immunol* 185(11):6413. <https://doi.org/10.4049/JIMMUNOL.1001829>.
- [45] Yeh, W.C., Cao, Z., Classon, M., McKnight, S.L., 1995. Cascade regulation of terminal adipocyte differentiation by three members of the C/EBP family of leucine zipper proteins. *Genes Dev* 9(2):168–181. <https://doi.org/10.1101/GAD.9.2.168>.
- [46] Hamm, J.K., Park, B.H., Farmer, S.R., 2001. A role for C/EBPbeta in regulating peroxisome proliferator-activated receptor gamma activity during adipogenesis in 3T3-L1 preadipocytes. *J Biol Chem* 276(21):18464–18471. <https://doi.org/10.1074/JBC.M100797200>.
- [47] MacGillavry, H.D., Stam, F.J., Sassen, M.M., Kegel, L., Hendriks, W.T.J., Verhaagen, J., et al., 2009. NFIL3 and cAMP response element-binding protein form a transcriptional feedforward loop that controls neuronal regeneration-associated gene expression. *J Neurosci* 29(49):15542–15550. <https://doi.org/10.1523/JNEUROSCI.3938-09.2009>.
- [48] Watson, G., Ronai, Z., Lau, E., 2017. ATF2, a paradigm of the multifaceted regulation of transcription factors in biology and disease. *Pharmacol Res* 119: 347–357. <https://doi.org/10.1016/J.PHRS.2017.02.004>.
- [49] Huh, H.D., Kim, D.H., Jeong, H.-S., Park, H.W., 2019. Regulation of TEAD transcription factors in cancer biology. *Cells* 8(6):600. <https://doi.org/10.3390/CELLS8060600>.
- [50] Zenz, R., Eferl, R., Scheinecker, C., Redlich, K., Smolen, J., Schonhaller, H.B., et al., 2008. Activator protein 1 (Fos/Jun) functions in inflammatory bone and skin disease. *Arthritis Res Ther* 10(1). <https://doi.org/10.1186/AR2338>.
- [51] Kajimura, S., Seale, P., Kubota, K., Lunsford, E., Frangioni, J.v., Gygi, S.P., et al., 2009. Initiation of myoblast/brown fat switch through a PRDM16-C/EBP- $\beta$  transcriptional complex. *Nature* 460(7259):1154. <https://doi.org/10.1038/NATURE08262>.
- [52] Cypess, A.M., Kahn, C.R., 2010. Brown fat as a therapy for obesity and diabetes. *Curr Opin Endocrinol Diabetes Obes* 17(2):143–149. <https://doi.org/10.1097/MED.0B013E328337A81F>.
- [53] Arch, J.R.S., Ainsworth, A.T., 1983. Thermogenic and antiobesity activity of a novel beta-adrenoceptor agonist (BRL 26830A) in mice and rats. *Am J Clin Nutr* 38(4):549–558. <https://doi.org/10.1093/AJCN/38.4.549>.
- [54] Hao, L., Scott, S., Abbasi, M., Zu, Y., Khan, M.S.H., Yang, Y., et al., 2019. Beneficial metabolic effects of mirabegron in vitro and in high-fat diet-induced obese mice. *J Pharmacol Exp Therapeut* 369(3):419–427. <https://doi.org/10.1124/JPET.118.255778>.
- [55] Arch, J.R.S., 2011. Challenges in  $\beta$ 3-adrenoceptor agonist drug development. *Ther Adv Endocrinol Metab* 2(2):59. <https://doi.org/10.1177/2042018811398517>.
- [56] Werner, A.L., Travaglini, M.T., 2001. A review of rosiglitazone in type 2 diabetes mellitus. *Pharmacotherapy* 21(9):1082–1099. <https://doi.org/10.1592/PHCO.21.13.1082.34615>.
- [57] Nissen, S.E., Wolski, K., 2007. Effect of rosiglitazone on the risk of myocardial infarction and death from cardiovascular causes. *N Engl J Med* 356(24): 2457–2471. <https://doi.org/10.1056/NEJM0A072761>.
- [58] Seale, P., Kajimura, S., Yang, W., Chin, S., Rohas, L.M., Uldry, M., et al., 2007. Transcriptional control of brown fat determination by PRDM16. *Cell Metabol* 6(1):38–54. <https://doi.org/10.1016/J.CMET.2007.06.001>.
- [59] Uldry, M., Yang, W., St-Pierre, J., Lin, J., Seale, P., Spiegelman, B.M., 2006. Complementary action of the PGC-1 coactivators in mitochondrial biogenesis and brown fat differentiation. *Cell Metabol* 3(5):333–341. <https://doi.org/10.1016/J.CMET.2006.04.002>.
- [60] Balaz, M., Becker, A.S., Balazova, L., Straub, L., Müller, J., Gashi, G., et al., 2019. Inhibition of mevalonate pathway prevents adipocyte browning in mice and men by affecting protein prenylation. *Cell Metabol* 29(4):901–916. <https://doi.org/10.1016/J.CMET.2018.11.017> e8.
- [61] Markan, K.R., Boland, L.K., King-McAlpin, A.Q., Clafin, K.E., Leaman, M.P., Kemerling, M.K., et al., 2020. Adipose TBX1 regulates  $\beta$ -adrenergic sensitivity in subcutaneous adipose tissue and thermogenic capacity in vivo. *Mol Metabol* 36. <https://doi.org/10.1016/J.MOLMET.2020.02.008>.
- [62] Lee, S., Benvie, A.M., Park, H.G., Spektor, R., Harlan, B., Brenna, J.T., et al., 2022. Remodeling of gene regulatory networks underlying thermogenic stimuli-induced adipose beiging. *Commun Biol* 5(1):1–16. <https://doi.org/10.1038/s42003-022-03531-5>, 5:1.
- [63] Sun, W., Dong, H., Balaz, M., Slyper, M., Drokhyansky, E., Colletuori, G., et al., 2020. snRNA-seq reveals a subpopulation of adipocytes that regulates thermogenesis. *Nature* 587(7832):98–102. <https://doi.org/10.1038/s41586-020-2856-x>.
- [64] Chen, Y., Ikeda, K., Yoneshiro, T., Scaramozza, A., Tajima, K., Wang, Q., et al., 2018. Thermal stress induces glycolytic beige fat formation via a myogenic state. *Nature* 565(7738):180–185. <https://doi.org/10.1038/s41586-018-0801-z>, 565:7738.
- [65] Wang, H., Liu, L., Lin, J.Z., Aprahamian, T.R., Farmer, S.R., 2016. Browning of white adipose tissue with roscovitine induces a distinct population of UCP1 + adipocytes. *Cell Metabol* 24(6):835–847. <https://doi.org/10.1016/J.CMET.2016.10.005>.
- [66] Haakonsson, A.K., Madsen, M.S., Nielsen, R., Sandelin, A., Mandrup, S., 2013. Acute genome-wide effects of rosiglitazone on PPAR $\gamma$  transcriptional networks in adipocytes. *Mol Endocrinol* 27(9):1536–1549. <https://doi.org/10.1210/ME.2013-1080>.
- [67] Step, S.E., Lim, H.W., Marinis, J.M., Prokesch, A., Steger, D.J., You, S.H., et al., 2014. Anti-diabetic rosiglitazone remodels the adipocyte transcriptome by redistributing transcription to PPAR $\gamma$ -driven enhancers. *Genes Dev* 28(9): 1018–1028. <https://doi.org/10.1101/GAD.237628.114>.
- [68] Chen, D., Parker, T.M., Bhat-Nakshatri, P., Chu, X., Liu, Y., Wang, Y., et al., 2021. Nonlinear relationship between chromatin accessibility and estradiol-regulated gene expression. *Oncogene* 40(7):1332–1346. <https://doi.org/10.1038/S41388-020-01607-2>.

- [69] Mitsui, S., Yamaguchi, S., Matsuo, T., Ishida, Y., Okamura, H., 2001. Antagonistic role of E4BP4 and PAR proteins in the circadian oscillatory mechanism. *Genes Dev* 15(8):995. <https://doi.org/10.1101/GAD.873501>.
- [70] Ikushima, S., Inukai, T., Inaba, T., Nimer, S.D., Cleveland, J.L., Look, A.T., 1997. Pivotal role for the NFIL3/E4BP4 transcription factor in interleukin 3-mediated survival of pro-B lymphocytes. *Proc Natl Acad Sci U S A* 94(6):2609–2614. <https://doi.org/10.1073/PNAS.94.6.2609>.
- [71] Keniry, M., Pires, M.M., Mense, S., Lefebvre, C., Gan, B., Justiano, K., et al., 2013. Survival factor NFIL3 restricts FOXO-induced gene expression in cancer. *Genes Dev* 27(8):916. <https://doi.org/10.1101/GAD.214049.113>.
- [72] Tong, X., Li, P., Zhang, D., VanDommelen, K., Gupta, N., Rui, L., et al., 2016. E4BP4 is an insulin-induced stabilizer of nuclear SREBP-1c and promotes SREBP-1c-mediated lipogenesis. *JLR (J Lipid Res)* 57(7):1219–1230. <https://doi.org/10.1194/JLR.M067181>.
- [73] Tong, Y., Zeng, P., Zhang, T., Zhao, M., Yu, P., Wu, B., 2019. The transcription factor E4bp4 regulates the expression and activity of Cyp3a11 in mice. *Biochem Pharmacol* 163:215–224. <https://doi.org/10.1016/J.BCP.2019.02.026>.
- [74] Ramakrishnan, S.K., Taylor, M., Qu, A., Ahn, S.-H., Suresh, M.v., Raghavendran, K., et al., 2014. Loss of von Hippel-Lindau protein (VHL) increases systemic cholesterol levels through targeting hypoxia-inducible factor 2 $\alpha$  and regulation of bile acid homeostasis. *Mol Cell Biol* 34(7):1208–1220. <https://doi.org/10.1128/MCB.01441-13>.
- [75] Kang, G., Han, H.S., Koo, S.H., 2017. NFIL3 is a negative regulator of hepatic gluconeogenesis. *Metab Clin Exp* 77:13–22. <https://doi.org/10.1016/J.METABOL.2017.08.007>.
- [76] Wang, Y., Kuang, Z., Yu, X., Ruhn, K.A., Kubo, M., Hooper, L.v., 2017. The intestinal microbiota regulates body composition through NFIL 3 and the circadian clock. *Science (New York, N.Y.)* 357(6354):912–916. <https://doi.org/10.1126/SCIENCE.AAN0677>.
- [77] Lee, B.C., Kim, M.S., Pae, M., Yamamoto, Y., Eberlé, D., Shimada, T., et al., 2016. Adipose natural killer cells regulate adipose tissue macrophages to promote insulin resistance in obesity. *Cell Metabol* 23(4):685–698. <https://doi.org/10.1016/J.CMET.2016.03.002>.
- [78] Higareda-Almaraz, J.C., Karbiener, M., Giroud, M., Pauler, F.M., Gerhalter, T., Herzig, S., et al., 2018. Norepinephrine triggers an immediate-early regulatory network response in primary human white adipocytes. *BMC Genom* 19(1). <https://doi.org/10.1186/S12864-018-5173-0>.
- [79] Pulit, S.L., Stoneman, C., Morris, A.P., Wood, A.R., Glastonbury, C.A., Tyrrell, J., et al., 2019. Meta-analysis of genome-wide association studies for body fat distribution in 694 649 individuals of European ancestry. *Hum Mol Genet* 28(1):166–174. <https://doi.org/10.1093/HMG/DDY327>.
- [80] Karlsson, T., Rask-Andersen, M., Pan, G., Höglund, J., Wadelius, C., Ek, W.E., et al., 2019. Contribution of genetics to visceral adiposity and its relation to cardiovascular and metabolic disease. *Nat Med* 25(9):1390–1395. <https://doi.org/10.1038/s41591-019-0563-7>, 25:9.